nature communications

Article

https://doi.org/10.1038/s41467-024-54157-6

A bitter anti-inflammatory drug binds at two distinct sites of a human bitter taste GPCR

Received: 6 May 2024

Accepted: 1 November 2024

Published online: 18 November 2024

Check for updates

Lior Peri[1,2,10], Donna Matzov[3,10], Dominic R. Huxley[4,10], Alon Rainish[1,2], Fabrizio Fierro[1,2], Liel Sapir[1,2,5], Tara Pfeiffer[6], Lukas Waterloo[6], Harald Hübner[6], Yoav Peleg[7], Peter Gmeiner[6,8], Peter J. McCormick[4,9], Dorothee Weikert[6,8] ✉, Masha Y. Niv[1,2] ✉ & Moran Shalev-Benami[3] ✉

Bitter taste receptors (TAS2Rs), a subfamily of G-protein coupled receptors (GPCRs) expressed orally and extraorally, elicit signaling in response to a large set of tastants. Among 25 functional TAS2Rs encoded in the human genome, TAS2R14 is the most promiscuous, and responds to hundreds of chemically diverse ligands. Here we present the cryo–electron microscopy (cryo-EM) structure of the human TAS2R14 in complex with its signaling partner gustducin, and bound to flufenamic acid (FFA), a clinically approved nonsteroidal anti-inflammatory drug. The structure reveals an unusual binding mode, where two copies of FFA are bound at distinct pockets: one at the canonical receptor site within the trans-membrane bundle, and the other in the intracellular facet, bridging the receptor with gustducin. Together with a pocket-specific BRET-based ligand binding assay, these results illuminate bitter taste signaling and provide tools for a site-targeted compound design.

Bitterness is elicited by the taste 2 receptor (TAS2R, class T) family. In humans, 25 functional TAS2Rs are encoded in the genome[1], that are typically classified as class A like GPCRs. However, TAS2Rs lack most family-A hallmark motifs, and share low sequence similarity both within the subfamily members and with other GPCRs[2]. TAS2Rs respond to a diverse array of tastants, and while some family members are narrowly tuned for specific ligands, others respond to agonists with remarkable chemical diversity[1,3,4]. TAS2R14 is a notable taste receptor that responds to the largest number of agonists, including vitamins[5], flavonoids[6], pharmaceuticals[7,8], and odorants[9]. TAS2R14 is abundant in the taste buds but is also expressed in extraoral tissues such as the respiratory[10,11], cardiovascular[12,13] and digestive[14] systems. Polymorphisms in the TAS2R14 gene were associated with cardiac physiology[13] and male infertility[15]. TAS2R14 overexpression was also documented in several types of cancer[12,16], and its stimulation was shown to elicit anti-proliferative and pro-apoptotic effects in multiple cancer cell lines[17–19]. In addition, individuals diagnosed with pancreatic adenocarcinoma that have elevated TAS2R14 expression levels show an extended overall survival compared to those with lower expression of the receptor[19]. These findings highlight TAS2R14 as a broadly-tuned receptor that responds to a large variety of ligands, and underscore potential therapeutic applications that go beyond bitter sensing.

Upon activation of TAS2Rs in taste cells, intracellular signaling is mediated through coupling to a specialized Gα protein called gustducin, that is primarily expressed in mammalian oral and intestinal tissues to mediate bitter, sweet and umami taste transduction[20].

[1]The Institute of Biochemistry, Food Science and Nutrition, Robert H. Smith Faculty of Agriculture, Food and Environment, The Hebrew University of Jerusalem, Rehovot, Israel. [2]The Fritz Haber Research Center, and the Harvey M. Kruger Center for Nanoscience & Nanotechnology, Institute of Chemistry, The Hebrew University, Jerusalem, Israel. [3]Department of Chemical and Structural Biology, Weizmann Institute of Science, Rehovot, Israel. [4]Centre for Endocrinology, William Harvey Research Institute, Barts and the London School of Medicine, Queen Mary, University of London, Charterhouse Square, London, UK. [5]Department of Chemistry, Bar-Ilan University, Ramat-Gan, Israel. [6]Department of Chemistry and Pharmacy, Medicinal Chemistry, Friedrich-Alexander-Universität Erlangen-Nürnberg, Erlangen, Germany. [7]Structural Proteomics Unit (SPU), Life Sciences Core Facilities (LSCF), Weizmann Institute of Science, Rehovot, Israel. [8]FAUNeW – Research Center New Bioactive Compounds, Friedrich-Alexander-Universität Erlangen-Nürnberg, Erlangen, Germany. [9]Department of Pharmacology and Therapeutics, Faculty of Health and Life Sciences, University of Liverpool, Liverpool, UK. [10]These authors contributed equally: Lior Peri, Donna Matzov, Dominic R. Huxley. ✉e-mail: dorothee.weikert@fau.de; masha.niv@mail.huji.ac.il; moransb@weizmann.ac.il

A recent cryo-EM structure of TAS2R46 bound to an agonist and a miniGα gustducin mimetic provided a snapshot of an active bitter taste receptor[21]. However, due to the large sequence variability of TAS2Rs and their highly varying ligand binding capacity, aspects regarding the mechanism of activation and ligand selectivity in this receptor family remain opaque.

Here we determine the structure of the active human TAS2R14 (hTAS2R14) in complex with miniG-gustducin and bound to flufenamic acid (FFA). FFA is a nonsteroidal anti-inflammatory molecule that acts via inhibition of cyclooxygenase-2 (COX2), and is also one of the most potent TAS2R14 agonists[8,22]. The structure reveals a dual binding mode of FFA to the receptor, where two copies of the agonist are bound at distinct receptor loci: one corresponds to the canonical binding site, located at the extracellular part of the receptor, and another is bound at the intracellular side, where it maintains interactions with TMs 3,5 and 7 and is also in direct contact with the alpha-5 helix of G-alpha gustducin. Through the design of a fluorescent FFA conjugate that, along with receptor labeling at either the extra- or intra-cellular sites allowed for the direct detection of the ligand's binding through Bioluminescence Resonance Energy Transfer (BRET), we further demonstrate the unusual dual binding mode of the ligand and highlight the intracellular pocket as a potential target for drug design.

Results and discussion

Overall description of the TAS2R14 constructs used for the structural studies

Full length hTAS2R14 was cloned into a baculovirus vector containing an N-terminal haemagglutinin (HA) signal peptide followed by a cleavable FLAG tag and the first 45 amino acids of rat somatostatin receptor 3 (SSTR3), that were previously shown to facilitate surface expression of TAS2Rs in mammalian cells[7]. For complex formation, we initially used a full-length human Gα-gustducin ($G\alpha_{gus}$), of which an ScFV16 epitope was introduced to the N-terminus by replacing the first 15 residues of wild-type gustducin with the corresponding amino-acids of $G\alpha i_1$ (iN15). ScFV16 was shown to stabilize G-protein heterotrimer formation in multiple complexes used for structural studies of GPCRs and is thus considered as a universal modulator for the heterotrimeric complex formation[23–26]. The receptor, $G\alpha_{gus}$-iN15 and Gβγ were co-expressed in insect cells and purified through tandem affinity steps in the presence of the TAS2R14 agonist FFA and ScFV16. However, despite the formation of a complex, the resulting assembly was highly unstable, and unsuitable for the cryo-EM studies.

We thus further created a miniGα-gustducin ($miniG_{gus}$) construct. The design was inspired by a previously described $miniG_i$[27], where the alpha-helical domain was replaced by an eight-residue linker, and seven mutations were added to confer stable protein expression (Supplementary Fig. 1a). To test construct activity, we used a split nanoluciferase assay, where the intracellular part of the receptor was fused to a large-BiT (LgBiT) segment, and the C- terminus of a soluble $miniG_{gus}$ was coupled to a small-BiT (SmBiT) fragment (Supplementary Fig. 1b-c)[24,28,29]. The proteins were overexpressed in mammalian cell lines, and signaling assays were performed in the presence of FFA at serial concentrations (Fig. 1g). The assay indicated a dose dependent response to FFA (EC_{50} = 46.26 ± 10 μM). To confirm the functionality of our $miniG\alpha_{gus}$ we also compared G-protein activity (Fig. 1h), using an optimized open-source bioluminescence resonance energy transfer (BRET) based system[30]. In brief, we used a Gα gustducin with a Renilla luciferase variant (RLuc8) inserted within the alpha-helical region along with an unlabelled beta subunit and a gamma subunit with GFP2 inserted at the N-terminus. This BRET-based system has been calibrated for optimal detection of agonist-induced heterotrimer dissociation[30,31]. Despite the difference in design of the complementation and the BRET dissociation assays, we obtained similar concentration response curves (Fig. 1g and Fig. 1h).

For the cryo-EM studies, we used a modified version of the mammalian constructs that also included the beta-gamma subunits. Here, an enhanced affinity SmBiT (HiBiT)[32] was fused to the N-terminus of the beta subunit and the gamma subunit was fused to the N-terminus of $miniG\alpha_{gus}$-iN15, as previously described for a G_q complex[25] (Supplementary Fig. 1d, e). Complex formation was induced by supplementing micromolar concentrations of FFA to insect cells co-expressing the constructs. We then used single-particle cryo-EM to

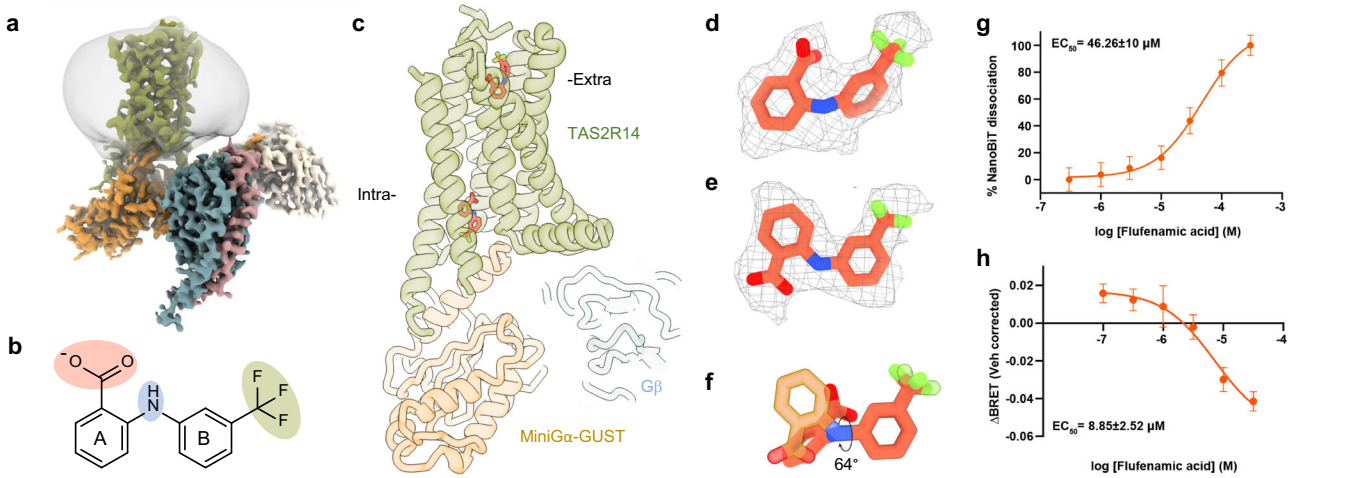

Fig. 1 | An overall description of the TAS2R14 complex. a Cryo-EM map of hTAS2R14 bound to the gustducin heterotrimer. TAS2R14 is colored green, gustducin in gold, the beta-gamma subunits are in teal and pink, respectively, and ScFV16 in white. **b** The chemical structure of FFA. The ring with the carboxylic moiety (red) is denoted A, and the ring with the trifluoromethyl moiety (green) is denoted B. The amino linker is highlighted in blue. **c** Cartoon representation of the TAS2R14 complex with FFA bound at the canonical (extracellular, extra-) and intracellular (intra-) sites. Colors are as in (**a**). **d** FFA docked in density for the canonical site. **e** FFA in density for the intracellular site. **f** Superposition of the canonical (orange) vs. the intracellular (gold) conformations of FFA indicating a 64° rotation of ring A relative to ring B. **g** Dose response curve for FFA in the mini-gustducin complementation assay designed for this study. Response is measured as nanoBiT dissociation normalized by basal activity of the wild-type receptor to FFA. Data are represented as mean ± SEM from three independent experiments performed in triplicate, indicating an EC_{50} of 46.26 ± 10 μM. **h** G-protein dissociation of TAS2R14 in response to FFA in HEK293 cells transiently co-expressing the wild-type receptor and TRUPATH biosensors for the full-length gustducin G-protein. Data are represented as mean ± SEM from seven independent experiments performed in triplicate, indicating an EC_{50} of 8.85 μM ± 2.52 μM. Source data are provided as a Source Data file.

https://doi.org/10.1038/s41467-024-54157-6

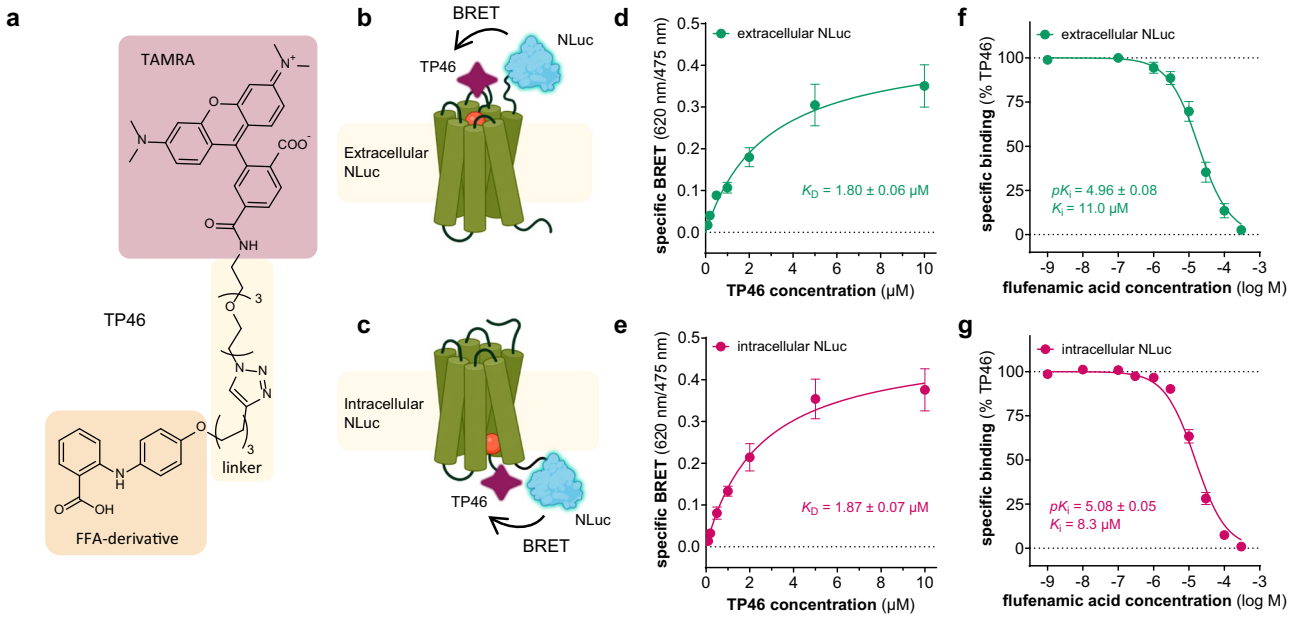

Fig. 2 | NanoBRET-based ligand binding assays for the extra- and intracellular binding pockets of TAS2R14. a Chemical structure of the fluorescent molecular probe TP46. **b**, **c** Schematic representation of the NanoBRET-based assay principle for the (**b**) extracellular and (**c**) intracellular NLuc-labeled TAS2R14. **d**, **e** Specific binding of TP46 determined in NanoBRET saturation binding assays reveals similar affinities for the intra- and extracellular binding pockets. Specific BRET was calculated as the difference in total BRET and non-specific binding determined in the presence of 30 μM FFA. Data are shown as mean ± SEM derived from $n = 5$ (extracellular, **d**) or $n = 7$ (intracellular, **e**) individual experiments. **f**, **g** Competition binding experiments with TP46 and FFA show binding affinities (K_i) of 11 μM and 8.3 μM, for the extracellular (**f**) and intracellular (**g**) sites, respectively. Data were normalized to total (100%) and non-specific binding (0%) and show mean ± SEM of $n = 7$ and 16 individual experiments, for the extracellular and intracellular NLuc constructs, respectively. Source data are provided as a Source Data file. Created in BioRender. BioRender.com/j19r877.

obtain a three-dimensional reconstruction of the hTAS2R14-miniG_{gus}βγ complex at a nominal resolution of 2.7 Å (Fig. 1, Supplementary Fig. 2 and 3, and Table S1). The map revealed the architecture of all complex components, as well as the mode of receptor association with gustducin and the agonist binding pose at the canonical binding site (Fig. 1d). Unexpectedly, we found an additional copy of the agonist bound at a distinct pocket facing the intracellular receptor interface (Fig. 1c, e). The ligand directly interacts with both the αN5 of gustducin and helices 3, 5 and 7 of the receptor.

FFA binds TAS2R14 at two distinct binding pockets

Our cryo-EM analysis revealed a structure in which two molecules of FFA are bound to the receptor simultaneously at both an extracellular site, as well as at an intracellular facet. As FFA has an amphiphilic nature, and is known to target cyclooxygenase (COX) intracellularly to maintain its anti-inflammatory actions, there exists a plethora of information regarding the cellular permeability of this molecule[33]. Thus, in principle, targeting the receptor intracellularly by this ligand is possible. However, to directly investigate the binding of FFA to TAS2R14, we established a BRET-based ligand binding assay. In this assay, we fused TAS2R14 to the small and bright nanoluciferase (Nluc) enzyme[34,35], either at the receptor's N- or C-terminius to facilitate a BRET-based binding assay we developed a suitable fluorescent FFA derivative. This was done using the available structure-activity relationships (SARs)[22,36]. We designed the position of the fluorophore to be via the meta- or para-positions of the aniline ring B of FFA. Hence, we synthesized a small set of fluorescent derivatives, that comprised linkers of different lengths and polarities that were connected to an azide- or alkyne-functionalized tetramethyl-rhodamine dye (TAMRA-5 or TAMRA-6) employing click chemistry[37] (Supplementary Fig. 4). This fluorophore has been successfully employed for NanoBRET-based ligand binding assays at intra- and extracellular binding pockets of various GPCRs[38–41]. We then screened membranes from HEK293T cells that were over-expressing the N- or C-terminally labeled TAS2R14-nanoluciferase constructs and identified TP46 as the most promising candidate specifically binding to both, the intra- and extracellular binding pockets (Fig. 2 and Supplementary Fig. 5). Notably, while TP46 could not be investigated for TAS2R14 activation due to its fluorescent nature interfering with the assays' read-outs, the alkyne precursor LW384 was found to be a partial agonist with an E_{max} of 66% relative to FFA (Supplementary Fig. 5), suggesting that the addition of the flexible alkyne linker to the para position of ring B is compatible with G-protein coupling to TAS2R14. Saturation binding experiments with TP46 and the extracellularly labelled Nluc-TAS2R14 or the intracellularly labelled TAS2R14-Nluc construct showed typical hyperbolic ligand binding profiles and revealed similar affinities of TP46 for both receptor-Nluc fusion proteins ($K_D^{extracellular}$ 1.80 μM; $K_D^{intracellular}$ 1.87 μM; Fig. 2d, e). Employing TP46 as the molecular probe in competition binding experiments, we determined the affinity of FFA to both ligand binding sites of TAS2R14. Displacement of TP46 with FFA was detected for both TAS2R14-Nluc fusion receptors, demonstrating binding affinities in the low micromolar range of FFA for both the extracellular (K_i 11 μM) and the intracellular (K_i 8.3 μM) sites (Fig. 2f, g). The experiments show that the TAMRA-labeled probe TP46 is capable of binding to two distinct sites of TAS2R14 which was detected by nanoBRET with N-terminal and C-terminal receptor-nanoluciferase fusion proteins, respectively. Our competition assays further showed that FFA specifically displaces TP46 and results in a reduced BRET signal from both TAS2R14-NLuc constructs, and thus directly support our observations from the EM-density maps that indicated binding of FFA to TAS2R14 at both the canonical and the intracellular pockets.

Very recently, two other studies revealed the TAS2R14 structure in complex with the synthetic FFA derivative cmpd28.1[42], FFA and aristolochic acid (AA)[43]. In these examples, the ligands were reported to bind at the intracellular, but not at the extracellular pocket. Instead, a cholesterol molecule was identified within the extracellular site. The

https://doi.org/10.1038/s41467-024-54157-6

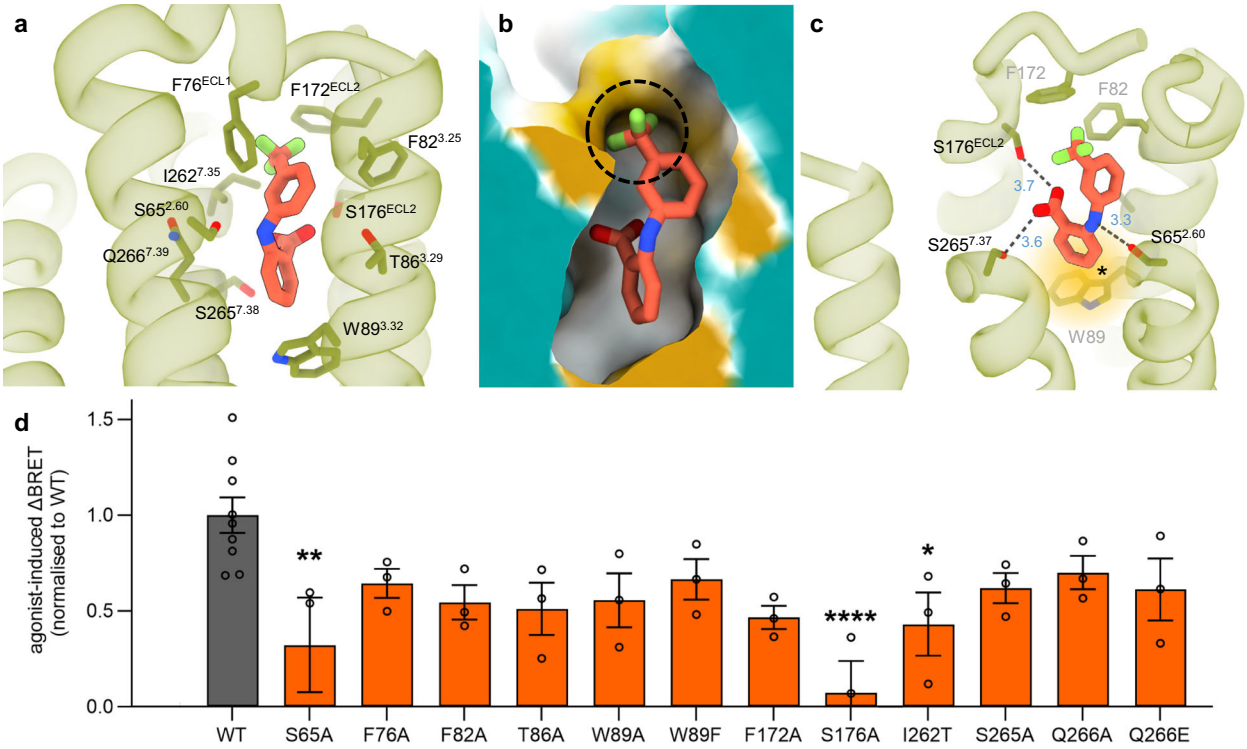

Fig. 3 | FFA binding at the canonical pocket. a FFA in the TAS2R14 extracellular binding pocket. The receptor is presented in light green, FFA in orange. Residues in the binding pocket are labeled and shown as sticks. **b** Ring B of FFA engages a hydrophobic cavity within the canonical binding pocket. Protein surface is mapped by lipophilicity, with hydrophilic residues colored in cyan and lipophilic areas in gold. The area near the trifluoromethyl moiety is circled with a dashed black line. **c** FFA interactions in the TAS2R14 binding pocket. Colors are as in (**a**). Dashed lines indicate bonds with distances in Å noted in blue. Perpendicular stacking interactions between ring B and W89$^{3.32}$ are highlighted in yellow and marked by an asterisk. **d** TAS2R14–G_{gust} activation responses in wild-type (WT) and canonical binding pocket mutants upon stimulation with $10^{-4.5}$ [M] FFA. Raw ΔBRET values were calculated from concentration-response curves (Supplementary Fig. 7) and normalized to WT. Ordinary one-way ANOVA with Dunnett's test for multiple comparison analysis with reference to WT. Data are mean ±SEM of n = 3 individual experiments performed in triplicate. Individual data points are depicted. $^{****}P < 0.0001$, $^{***}P < 0.001$, $^{**}P < 0.01$, $^{*}P < 0.05$. Source data are provided as a Source Data file.

origin of cholesterol in these studies[42,43] may stem from the hydrolysis of cholesteryl-hemisuccinate (CHS) that was used in excess during protein purification steps[42]. In contrast, our structure, which was obtained using lower concentrations of CHS during the purification, suggests binding of two copies of FFA at both the extracellular and intracellular sites. A thorough structural comparison shown in Supplementary Fig. 6 indicates that FFA does not correspond by shape and/or location to the cholesterol density observed in the other studies, and vice versa. Another recent study indicated the binding of cmpd28.1 at both sites[44] and is consistent with our findings (Supplementary Fig. 6).

To further explore the role of cholesterol in mediating TAS2R14 activity, we used our NanoBRET assay and tested binding of TP46 to each individual site at elevated cholesterol concentrations (Supplementary Fig. 6j,k). Our results show that within the extracellular pocket, cholesterol can substitute TP46 at millimolar concentrations (Supplementary Fig. 6j), concentrations that are two orders of magnitude higher than FFA. This suggests that while cholesterol can occupy the site, FFA is more likely to do so when present. Notably, at the intracellular pocket, binding experiments conducted with TP46 and cholesterol show an enhancement of TP46 binding to the intracellular site in the presence of cholesterol, suggesting a possible positive allosteric action of cholesterol on TAS2R14 (Supplementary Fig. 6k). This is in agreement with other studies showing that cholesterol modulates GPCR activity through allosteric sites located inside and outside the 7TM bundle[45–48]. Indeed, in our cryo-EM maps, we observe three densities that may correspond to cholesterol bound to the receptor at the interface with the membrane lipids (Supplementary Fig. 6i). Altogether, our studies suggest a rather complex binding mode to this promiscuous receptor, by which different ligands can activate the receptor in distinct ways.

Description of FFA in the canonical binding pocket

TAS2R14 is activated by a large array of chemically diverse ligands[4,22,49]. FFA is among the most potent reported TAS2R14 agonists, and activates the receptor at micromolar concentrations (Fig. 1g-h)[22]. Chemically, FFA consists of two aromatic rings, often referred to as ring A and ring B, that are modified with carboxylic acid and trifluoromethyl moieties, respectively (Fig. 1b).

In the cryo-EM structure, FFA engages the canonical binding pocket with the trifluoromethyl moiety pointing towards the extracellular milieu, where it faces a hydrophobic cavity composed of F76^{ECL1}, F82$^{3.25}$, F172^{ECL2} and I262$^{7.34}$ (numbers in subscript correspond to Ballesteros–Weinstein (BW) numbering[50]; Fig. 3a, b). To test the contribution of the hydrophobic interface to FFA engagement with the receptor, we designed three phenylalanine to alanine substitutions in TAS2R14, namely, F76A^{ECL1}, F82A$^{3.25}$ and F172A^{ECL2}, and tested the ability of the receptor to stimulate the G-protein complex in the presence of FFA through our BRET signaling assay (Fig. 3d and Supplementary Figs. 7 and 8). Our results indicate that these point mutations did not significantly alter the receptor's activation. Notably, alanine substitution at position F82$^{3.25}$ did not have a significant effect on signaling. This is unusual, as the 3.25 position in class A GPCRs is known to be a major determinant of the orthosteric binding pocket geometry and is crucial for agonist binding and signal initiation[24,51,52]. While in most GPCRs 3.25 encompasses a cysteine residue engaged in a disulfide

https://doi.org/10.1038/s41467-024-54157-6

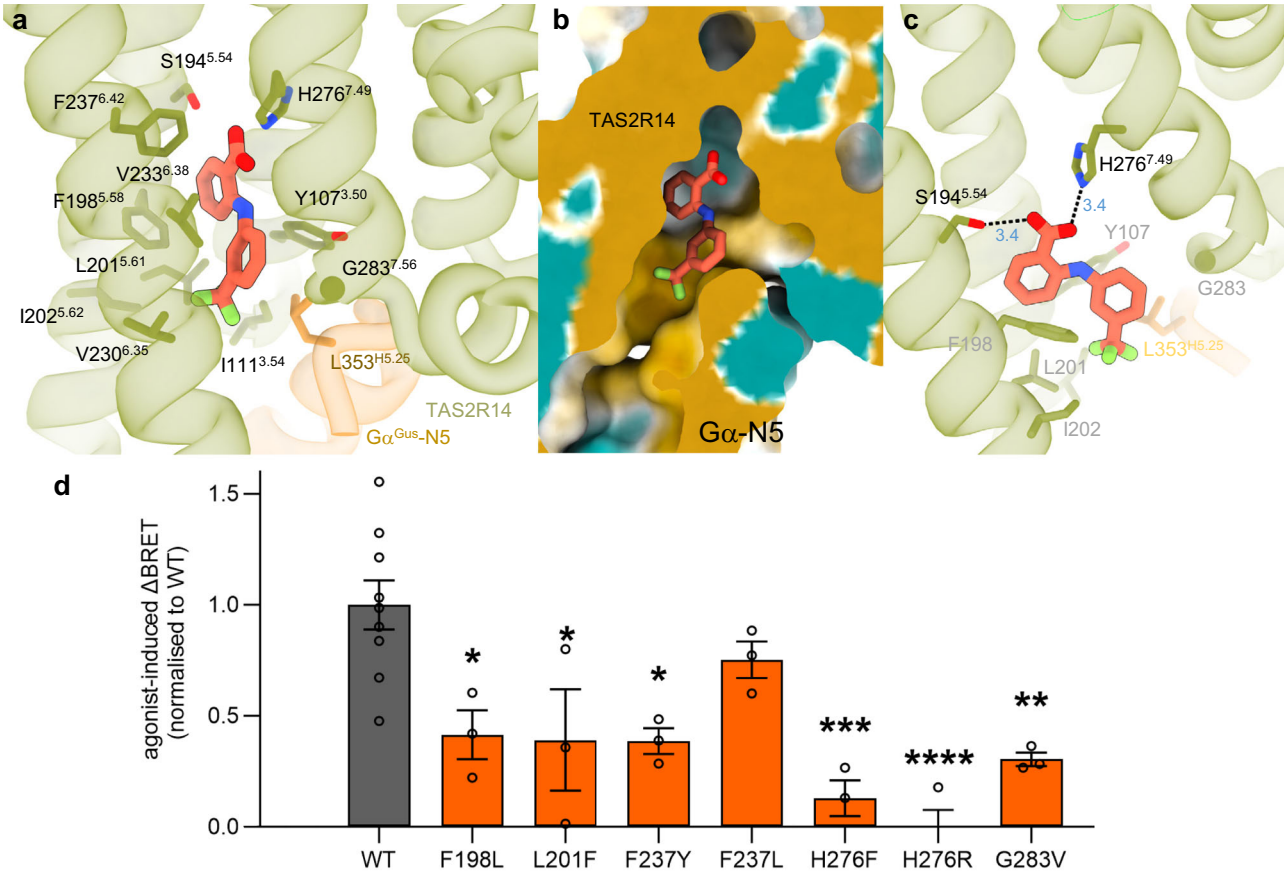

Fig. 4 | FFA binding in the intracellular pocket. a FFA binding pose at the intracellular site. The receptor is colored light green, gustducin in gold and FFA in orange. Residues in the binding pocket are labeled and shown as sticks. **b** Ring B of FFA engages a hydrophobic pocket composed of TMs 3, 5 and 7 and the α5 helix of gustducin. Protein surface is mapped by lipophilicity, with hydrophilic residues in cyan and lipophilic areas in gold. The α5 helix of gustducin is labeled. The hydrophobic pocket surrounding the trifluoromethyl moiety in FFA is circled. **c** FFA interactions in the TAS2R14 binding pocket. Protein and FFA colors are as in panel (**a**). Dashed lines indicate hydrogen bonds with distances in Å noted in blue. **d** TAS2R14–G_{gust} activation responses in wild-type (WT) and intracellular binding pocket mutants upon stimulation with $10^{-4.5}$ [M] FFA. Raw ΔBRET values were calculated from concentration-response curves (Supplementary Fig. 7) and normalized to WT. Ordinary one-way ANOVA with Dunnett's test for multiple comparison analysis with reference to WT. Data are mean ±SEM of n = 3 individual experiments performed in triplicate. Individual data points are depicted. $^{****}P < 0.0001$, $^{***}P < 0.001$, $^{**}P < 0.01$, $^{*}P < 0.05$. Source data are provided as a Source Data file.

bridge, position 3.25 in TAS2Rs is highly variable, suggesting that its function is not conserved in the taste receptor family (Supplementary Fig. 9). Mutation I262T at position 7.35 showed slightly lowered activity, possibly suggesting the importance of a bulky hydrophobic amino acid at that position.

Ring A in FFA harbors a carboxylic acid moiety that is facing a cavity enriched with polar residues, including S65$^{2.60}$, T86$^{3.29}$, S176^{ECL2}, S265$^{7.38}$, and Q266$^{7.39}$, and maintains direct contacts with the serine residues 176 and 265 of ECL2 and TM 7, respectively (Fig. 3c). S65$^{2.60}$ makes polar interactions with the amine linker that connects A and B rings in FFA (Fig. 3c).

To test the influence of polar contacts on FFA binding, we designed a set of mutations, namely, S65A$^{2.60}$, S176A^{ECL2} and S265A$^{7.37}$. Additionally, we added T86$^{3.29}$A/S mutations, that in previous studies demonstrated significantly reduced susceptibility to FFA[53] and Q266$^{7.39}$A/E that did not. Notably, an S176^{ECL2} substitution to alanine abrogated receptor function (Fig. 3d) highlighting the role of ECL2 in function of the receptor. The S65A$^{2.60}$ mutation significantly impacted activation by FFA when compared with the wild-type receptor, implying a role for this position in ligand-receptor interactions or receptor functionality (Fig. 3d).

Ring A is further extended towards the receptor's core and maintains perpendicular aromatic stacking with W89$^{3.32}$ (Fig. 3c). W$^{3.32}$ is mostly conserved in TAS2Rs (84%), (Supplementary Fig. 9) and is thought to play an important role in receptor activation[21]. Previous work by Nowak et al.[53] showed limited effect of the TAS2R14 W89A$^{3.32}$ mutation on the EC_{50} of FFA while an W89F$^{3.32}$ substitution remained unaffected. Similarly, our signaling assay does not show a significant change in response to FFA in the 3.32 mutants (Fig. 3d). In addition, no change in receptor expression was observed while compared with the wild-type construct (Supplementary Fig. 8), demonstrating that despite the high level of conservation, substitutions at position 3.32 in TAS2R14 did not alter the receptor's ability to fold, migrate to the cell surface or signal. Notably, an alanine substitution at the synonymous positions in TAS2R10, TAS2R38, TAS2R44 and TAS2R46 impaired the receptors' responses to a large array of tastants[21,54,55]. This data suggests that compared with other members of the TAS2R family, W$^{3.32}$ in TAS2R14 does not seem to play a significant role in receptor activation by at least some of its ligands, such as FFA. A plausible explanation for the discrepancy could be the second binding pocket for FFA, found through these studies, that could serve as an alternative mechanism for receptor activation.

Description of FFA binding to the intracellular binding site

In addition to the ligand at the canonical site, we found an additional density that bridged the αN5 of gustducin with TMs 3, 5, and 7 (Figs. 1e and 4). A copy of FFA could be fitted unambiguously to this density while occupying a conformation that is distinct to the canonical pocket

https://doi.org/10.1038/s41467-024-54157-6

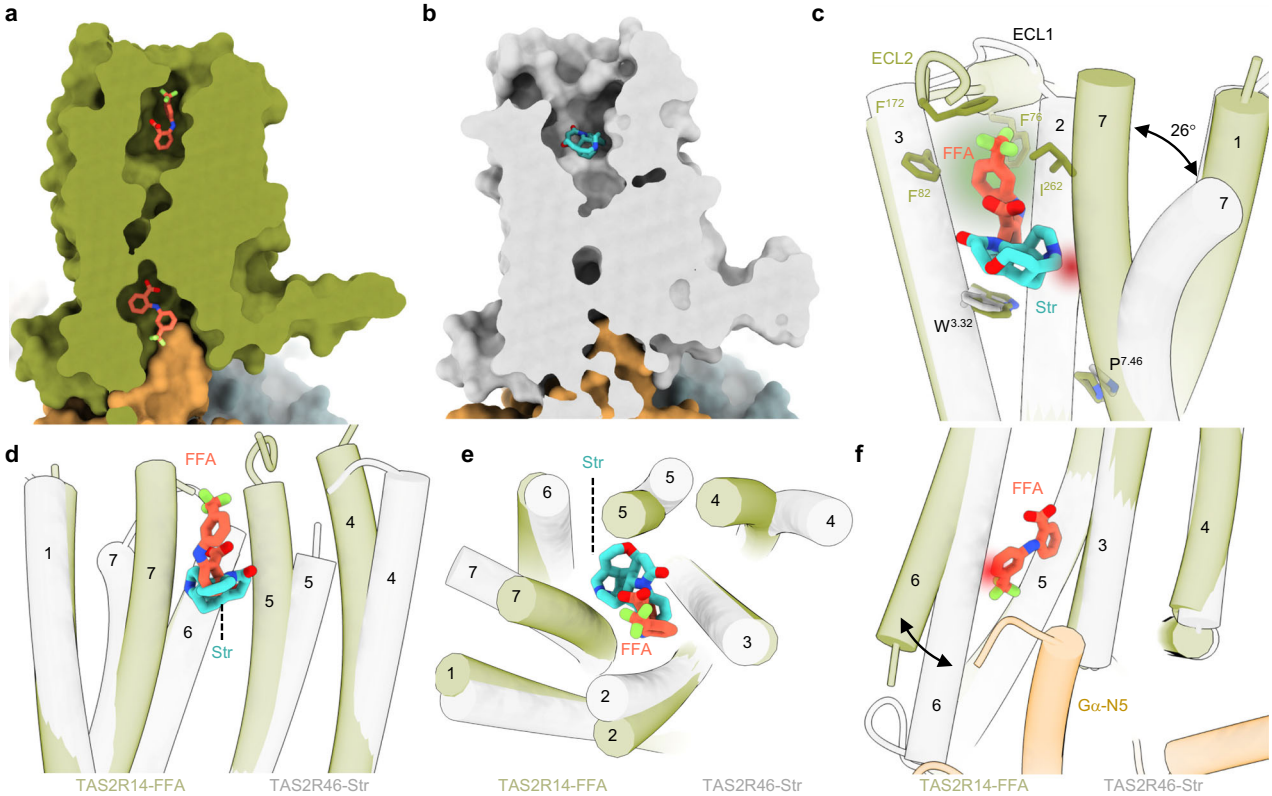

Fig. 5 | Comparison of TAS2R14 with TAS2R46. a, **b** A view of FFA (orange, **a**) and strychnine (Str, cyan, PDB 7XP6, **b**) at the TAS2R binding pocket. TAS2R14 is in green (**a**), and TAS2R46 in gray (**b**) Gustducin is shown in gold for both receptors. **c** Superposition of FFA and Str within the canonical binding pocket reveals different binding modes for the two ligands. FFA extends into a cavity localized towards the extracellular milieu. The cavity is highlighted in green and composes the hydrophobic pocket that accommodates the trifluoromethyl moiety. Str clashes with the inward TM7 position of TAS2R14, thus there is an outward movement of TM7 at the extracellular site. The clash is presented in red. Residue and helix numbers are indicated in the figure. TAS2R14 is green, TAS2R46 is grey. **d**, **e** Comparison of TM arrangement in the canonical binding pocket reveals major changes in the orientation of TMs 2,4,5 and 7 in the bound structures of TAS2R14 (green) and TAS2R46 (gray). A side view is in (**d**), top view is presented in (**e**). **f** Superposition of TAS2R14 (green) and TAS2R46 (gray) reveals that in the intracellular face, TM arrangement is identical for both receptors, apart from an outward movement of TM6 in TAS2R14. A clash with TM6 position in TAS2R46 (that lacks the second pocket) is indicated in red.

(Fig. 1e,f). In this conformation, ring A in the intracellular location is rotated 64° with respect to the same ring at the canonical site (Fig. 1f). This binding pose was further validated by Gemspot[56] and was also found to be stable through our MD simulations (Supplementary Fig. 10 and Supplementary Tables 2 and 3). The pose corresponds well with the recent study showing FFA binding to the intracellular site of TAS2R14[43] (Supplementary Fig. 6g). In this site, the trifluoromethyl moiety is oriented towards the intracellular face of the receptor and is surrounded with hydrophobic residues of TMs 3, 5 and 7, namely: $I111^{3.54}$, $F198^{5.58}$, $L201^{5.61}$, $I202^{5.62}$, $V230^{6.35}$ and $V233^{6.38}$ (Fig. 4a,b). This hydrophobic cavity is further capped with $L353^{gus\cdot5.25}$ of Gα gustducin (residue numbering in mini-gustducin corresponds to the wild-type human gustducin sequence), and with $Y107^{3.50}$. The carboxyl moiety in ring A is maintaining hydrogen bonds with $S194^{5.54}$ and $H276^{7.49}$. We selected a set of seven mutations surrounding the intracellular binding pocket in TAS2R14, $F198L^{5.58}$, $L201F^{5.61}$, $F273Y/F273L^{7.46}$, $H276F^{7.49}$/$H276R^{7.49}$, and $G283V^{7.56}$ (Fig. 4d) and performed BRET signaling assays to test the receptor susceptibility to FFA. The $F198L^{5.58}$ (rs202123922) and $L201F^{5.61}$ (rs35804287) are natural variants in humans, where $L201F^{5.61}$ was reported to reduce the receptor's sensitivity to agonists[13]. The corresponding positions in TAS2Rs are mostly conserved (Supplementary Fig. 9). For the natural variants, we found that both led to a reduced G-protein activation (Fig. 4d), most likely due to their direct interaction with FFA. While the $F273^{7.46}$ substitutions had minor effects on activation, the $H276^{7.49}$ substitutions were deleterious for signal instigation. Position 7.49 is a conserved histidine residue in 24 out of 25 TAS2Rs (Supplementary Fig. 9) and composes the $H^{7.49}S^{7.50}xxL^{7.53}$ motif, that is synonymous to $N^{7.49}P^{7.50}xxY^{7.53}$ in class A GPCRs[2]; our results further highlight the importance of this residue to receptor activation. To further monitor FFA binding to the intracellular pocket, a $G283V^{7.53}$ mutation was created and was expected to restrict pocket accessibility due to steric hindrance. This mutant was indeed found to significantly reduce receptor activation.

Altogether, the effects of mutations in the intracellular pocket were more pronounced compared with the extacellular receptor site, highlighting this pocket as a main site of activation for TAS2R14.

Comparison of TAS2R14 with other taste receptors

TAS2Rs are a highly diverse and promiscuous family of receptors that responds to a large number of variable tastants[4]. An earlier study determined the structure of another bitter taste receptor, TAS2R46, in complex with the alkaloid, strychnine[21]. The comparison of the two structures shows that despite belonging to the same sub-family, the receptors share very little in regards to ligand binding (Fig. 5).

At the canonical pocket, the structures greatly differ both in shape and volume of the cavity; While TAS2R14 has a rather narrow void, TAS2R46 has a wide opening that is also more exposed to the extracellular milieu (surface areas are 426 Å^3 and 511 Å^3 for TAS2R14 and TAS2R46, respectively; Fig. 5a, b and Supplementary Table 4). Within the pocket, FFA and strychnine, that differ in their chemical structure and composition, have limited overlap and occupy different regions of their respected cavities (Fig. 5c). Strychnine has an overall spherical

https://doi.org/10.1038/s41467-024-54157-6

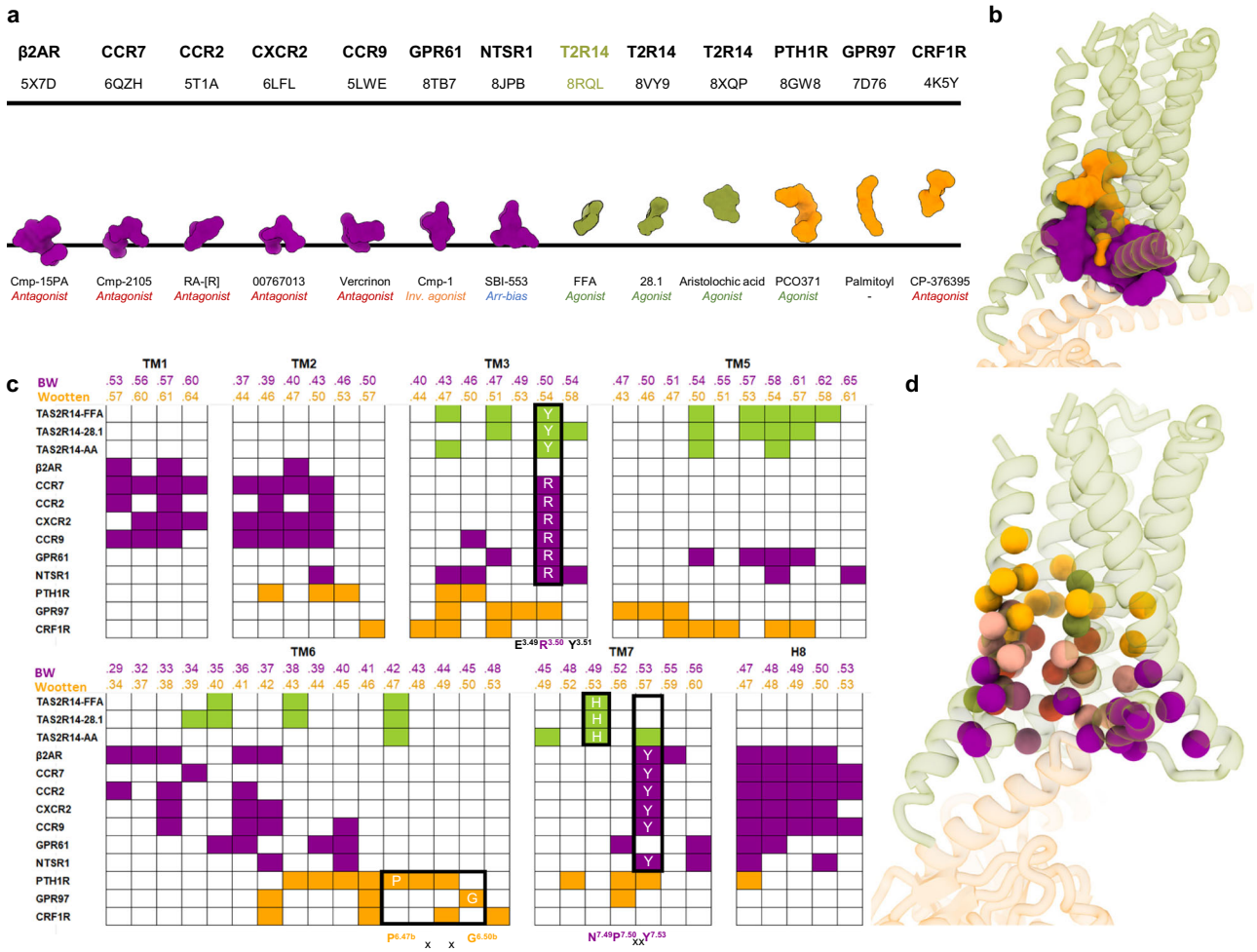

Fig. 6 | Comparison of the TAS2R secondary binding site with intracellular pockets of other GPCRs. a Localization of ligands targeting intracellular binding pockets in GPCRs. The black lines represent the membrane boundaries and are used as a reference to show that different ligands occupy slightly different interfaces within the intracellular cavity. Colors indicate family affiliation, with class A in magenta, class T (taste) in green, and class Bin gold. GPCR identity and PDB ID are labeled on top of the scheme. The bottom labels indicate the ligand name and reported activity (agonist/antagonist/inverse agonist). **b** Representation of ligand position in the intracellular site in 3D. Structures were superposed to TAS2R14 (aligned on TM4). Similar to the 2D scheme in (**a**), the superposition shows that class B binders (gold) occupy a higher position in the pocket when compared with class A binders (magenta). FFA (green) is similar to class A in regard to the positioning within the pocket. **c** Characterization of the residues within the intracellular binding pocket. Residues shown are within 4 Å distance from their respective ligands. Receptor names are indicated to the left; BW (class A) and Wootten (class B) numbering of residues in their respective TMs are on top of each column. Colors are according to family affiliation and are as in (**a**). Conserved positions or positions that appear in most pockets are also indicated by the relevant amino-acid letter code. **d** Representation of residues involved in ligand binding in the intracellular pocket in 3D. Residues that are strictly interacting with class A, B, or TAS2R14 are in their respected colors (magenta, gold and green). Residues that participate in the binding of all reported ligands are in red. Residues that participate in more than one receptor class, but not all, are in pink.

shape and is packed at the bottom of the pocket stacking against a conserved tryptophan residue at position 3.32 ($W88^{3.32}$ in TAS2R46, Supplementary Fig. 9). In contrast, FFA, that has an elongated shape, is oriented in a perpendicular orientation (maintaining interactions with the corresponding residue, $W89^{3.32}$, in TAS2R14) and extends towards the extracellular space while interacting with a hydrophobic cavity composed of non-conserved residues of ECL1, ECL2 and the tips of TMs 3 and 7 (Fig. 5c). This cavity is formed by different arrangement of the extracellular surroundings in TAS2R14, that includes the packing of the extracellular loops towards the receptor's core along with an inward-inclined arrangement of TMs 4, 5, and 7 at the extracellular face (Fig. 5c–e, Supplementary Fig. 11a). TM2 is also slightly shifted outwards in comparison with TAS2R46 structure, creating space that accommodates ring B of FFA (Fig. 5e).

The most notable difference in the extracellular TM arrangement is the TM7 position (Fig. 5c and Supplementary Fig. 11a). In both receptors TM7 has a kink, that is caused by a hinge originating from a shared proline residue in position 7.46 ($P273^{7.46}$ and $P272^{7.46}$ in TAS2R14 and TAS2R46, respectively; (Supplementary Fig. 9). However, the tilt level greatly differs, with only a mild tilt (22°) for TAS2R14, and a 45° tilt in TAS2R46, that profoundly opens the extracellular space of the receptor and contributes to the larger void of the binding pocket (Fig. 5c–e and Supplementary Fig. 11a). Considering the differential binding mode of the two ligands within the pockets, it is tempting to speculate that the tilt level might depend on the ligand's geometry. Also, given that the proline residue ($P^{7.46}$) is conserved in most TAS2Rs (Supplementary Fig. 9), but not in other GPCRs, this could represent a common mechanism for bitter taste receptors. In fact, the odorant receptor family is the only other GPCR family with conserved $P^{7.46}$ (Supplementary Fig. 11b). This family of receptors also recognizes numerous and diverse ligands, which could further support the role of $P^{7.46}$ for versatility.

The most profound difference between the two receptors is that in TAS2R46, the ligand only binds at the extracellular pocket, and no

ligand is present in the intracellular site (Fig. 5a, b). Comparing the intracellular domain of the two receptors at the structural level, it is noticeable that while the extracellular sites exhibit a pronouncedly different TM rearrangement, the intracellular face is nearly identical, apart from an apparent displacement of TM6 outwards in the TAS2R14 structure (Fig. 5f). Notably, one significant difference is that position 7.50 in TAS2R14 is a serine (S277$^{7.50}$), while at TAS2R46, the orthologous residue is proline (P276$^{7.50}$, Supplementary Fig. 9). This position is a conserved proline in most GPCRs and composes the N$^{7.49}$P$^{7.50}$xxY$^{7.53}$ motif, a key signature motif in class A receptors that is crucial for the structural rearrangements of receptors during activation. In TAS2Rs, this motif is replaced by an H$^{7.49}$S/P$^{7.50}$xxL$^{7.53}$ consensus[2]. Position 7.50 is not in direct contact with FFA, but H$^{7.49}$, also part of the motif, is maintaining polar contacts with the ligand, and our mutational studies confirm the importance of this position (Fig. 4f, g). In regards with the G-protein contact, the overall conformation of the two receptors is nearly identical around the FFA secondary binding site, and so are the interactions with gustducin. However, at a more global level, the TM6 movement in TAS2R14 breaks two contacts between the receptor and the α5 helix of gustducin. Those include S220$^{6.27}$ in TAS2R46 that interacts with D341$^{gus\text{-}H5.13}$ and K345$^{gus\text{-}H5.17}$ and V223$^{6.30}$ that interacts with F354$^{gus\text{-}H5.26}$ (Supplementary Fig. 11c). While these positions are mostly conserved in TAS2Rs, they correspond to A222$^{6.27}$ and K225$^{6.30}$ in TAS2R14, respectively. Although these contacts are remote from the binding pocket, the fact that they are different in TAS2R14 compared with other TAS2Rs might change the tendency of TAS2R14 to bind gustducin at the interface, rendering TM6 more mobile and thus possibly more prone for ligand entry to the intracellular site.

This analysis shows that despite belonging to the same receptor class, the binding mode of tastants to bitter taste receptors is greatly diversified. A conservation analysis comparing all human class T receptors similarly illustrates that the extracellular pocket of TAS2R, with the exception of W$^{3.32}$, is highly variable amongst human TAS2Rs, while the intracellular site is more conserved (Supplementary Fig. 9b). The potential for at least some of the TAS2Rs to accommodate ligands at the intracellular site adds to the versatility and complexity of the TAS2R family.

Comparing the intracellular pocket with other reported intracellular ligands

Recent studies revealed the binding of small molecular ligands at the intracellular face of other GPCRs. Those include several class A members, the chemokine receptors (CCRs 2,7 and 9[57–59]), CXCR2[60], the orphan receptor GPR61[61], the β2 adrenergic receptor[62], and the neurotensin 1 receptor (NTSR1)[63], as well as the parathyroid 1 (PTH1R)[64,65] and the corticotropin releasing factor type 1 (CRF1R)[66] receptors, of class B. In addition, a palmitoyl moiety that is anchored to the αN5 helix of $G\alpha_o$ was also reported to occupy the same cavity in a structure of the adhesion GPCR (class B2) GPR97[67]. The present study revealed the binding of FFA to the intracellular face of the bitter receptor, TAS2R14, and other studies showed the binding of a synthetic derivative of FFA (cmpd28.1)[42–44] as well as of aristolochic acid (AA)[43] to target the same receptor pocket.

Superposition of the bound structures reveals that despite bearing very different chemical scaffolds, the ligands' positions largely overlap, where they jointly engage residues in TMs 3,5,6 and 7 of their respective receptors (Fig. 6a, b and Supplementary Fig. 12a, b). Within this relatively small set of compounds, class A binders extend towards the G-protein-receptor interface, thus engaging with distinct positions in TM1 and H8; whereas class B ligands are pointing towards the canonical binding site, maintaining interactions with residues at TMs 5 and 6 that are deeply penetrating the 7TM core towards the canonical binding site (Fig. 6a, b). As a result, the class A binders interact with both the D[E]$^{3.49}$R$^{3.50}$Y$^{3.51}$ and the N$^{7.49}$P$^{7.50}$xxY$^{7.53}$ motifs via R$^{3.50}$ and Y$^{7.53}$, respectively (Fig. 6c); these motifs are missing in class B. In contrast, class B ligands target the P$^{6.47b}$xxG$^{6.50b}$ motif that was found to be key for the structural rearrangement required for the activation of this class of receptors (Fig. 6). These results are also consistent with the recent binding mode reported for the FFA derivative cmpd28.1[42] and AA (Fig. 6). Common features include the interaction with Y$^{3.50}$ and H$^{7.49}$ of the F$^{3.49}$Y$^{3.50}$xxK$^{3.53}$ and the H$^{7.49}$S/P$^{7.50}$xxL$^{7.53}$ motifs, that are analogous to the D[E]$^{3.49}$R$^{3.50}$Y$^{3.51}$ and the N$^{7.49}$P$^{7.50}$xxY$^{7.53}$ motifs in class A, respectively[2].

Notably, for most reported structures, the ligands shown to bind the intracellular site, were only bound in a single copy to the intracellular domain, while the extracellular site remained unoccupied. An exception is the GPR97 structure, where in addition to the palmitoyl moiety, occupying the intracellular cavity, there is a sterol partial agonist, bound at the extracellular pocket (Supplementary Fig. 12c[67]). These results are in agreement with our NanoBRET results and with recent work[42,43] showing that cholesterol can also bind the extracellular site of TAS2R14 when added in high concentrations.

These results further indicate that intracellular site binders to GPCRs can have a range of pharmacological effects spanning from inverse-agonism[61] to biased[63] and full agonism[42,43] (Fig. 6a). This highlights the intracellular pocket, in some GPCRs, as likely to interact with yet unknown intracellular ligands. Such ligands could include endogenous ligands such as the palmitoyl moiety in adhesion GPCRs, as well as extracellular modulators that can permeate the cell membrane. Notably, probenecid, an FDA-approved medication for the treatment of Gout disease, that was shown to antagonize the activity of multiple bitter type receptors (e.g., TAS2R16, TAS2R38, and TAS2R43) was also suggested to target the intracellular facet of the taste receptor TAS2R16[68]. This work indicated that mutations in the intracellular side of TAS2R16 at positions 2.38 and 3.43 did not affect the response to receptor agonists, but significantly altered the antagonistic effect of probenecid[68]. Several tastants were shown to rapidly enter liposomes and taste cells[69]. Together with our findings, this suggests that the intracellular site can be a critical point for modulation of multiple GPCR families, expanding the possibilities of current hotspots in GPCR targeting, and may be of immense pharmacological interest.

In summary, our cryo-EM structure of TAS2R14 reveals two binding modes for FFA, one at the canonical (extracellular) binding site and another at the intracellular facet, where it interacts with key elements important for GPCR activation and with the intracellular partner gustducin. Our binding assay shows that FFA binds at both sites with similar affinities that are at the micromolar range, while cholesterol binds to the extracellular pocket at millimolar concentrations. The key role of the intracellular binding pocket, which is highlighted in several other GPCRs, is established for TAS2R14 via the combination of signaling and binding assays. Biologically, this pocket enables TAS2R14 to sense intracellular and membrane-permeating ligands. The findings pave the way to studying the complexity of GPCR signal integration across the membrane and to expanding the pharmacological space for targeted drug design and provide the tools for site-directed structure guided design for this receptor. This is not only important for understanding food sensing and evaluation, but is also critical for several diseases and disorders that are associated with TAS2R14 extra-oral expression.

Methods

Construct design and cloning

For structure determination, the full-length human TAS2R14 (hTAS2R14) cDNA modified with an N-terminal haemagglutinin (HA) signal peptide followed by a FLAG-tag and the first 45 amino acids of rat somatostatin receptor 3 (SSR3)[7] was cloned into pFASTBAC1 (Bac-to-Bac, Thermo Fisher Scientific). In further optimizations of this construct, a LgBiT[28] was also installed at the C-terminus of the receptor following a GSGSSGSGSS linker. Human mini$G\alpha_{gus}$ was designed based

on *Nehme* et al.[70] (Supplementary Fig. 1). In brief, the α-helical domain was deleted and replaced by a GGSGGSGG linker, Y230 and N241 were also removed and 7 single point mutations, namely, G42D, E43N, G217D, A226D, A229D, V332A, V335I were incorporated for construct stabilization (residue numbers are according to the wild-type human gustducin and sequence alignment is shown in Supplementary Fig. 1a). The N-terminus of MiniGα_{gus} was further modified with the first 15 amino acids of Gα_{i2} to allow for ScFV16 recognition. Followed by a GSSGGGGSGGGGSSG linker, Gγ_2 was cloned prior to mini Gα inserted under the P10 promotor in a pFastBac Dual vector. A 6x His N-terminally labeled human Gβ_1 with a C-terminal HiBiT was cloned into the same vector following a polyhedrin promotor.

Cloning was performed by restriction free method, as described in *Unger* et al.[71]. Primers are summarized in supplementary Table 5.

For signalling assays conducted in human embryonic kidney 293 (HEK293) cells, a miniGα_{gus} with an N-terminus SmBiT tag was inserted into pCDNA3.1. For the same studies, TAS2R14 that was N-terminally labeled with a 3xHA-tag, SSR3 and C-terminally fused to LgBiT was cloned into pCDNA3.1. Construct design was similar to the melanocortin 4 construct described in *Israeli* et al.[24] (Supplementary Fig. 1b).

For the TRUPATH assays, TAS2R14 was cloned into cDNA3.1 with an N-terminal FLAG-SSR3[7]. The same construct was also used for the mutagenesis studies and for the detection of surface expression levels using FACS analysis.

For the ligand binding BRET assays, an N-terminally modified Nluc-TAS2R14 sequence was cloned as previously described for secNluc-D3R[40] by PCR and Gibson assembly[72], leading to a fusion protein of a cleavable membrane export signal peptide followed by the nanoluciferase, a GSSG-linker sequence, and the hTAS2R14 coding sequence. The hTAS2R14 isoform with an additional amino terminal export tag consisting of a cleavable HA-signal peptide followed by a FLAG-tag and the first 45 amino acids of rat somatostatin receptor 3[7] was used to generate the C-terminally modified TAS2R14-NLuc fusion protein. This sequence was fused in frame with a 24 amino acid linker (ATGLRSRAQASNSAVDGTAGPVAT) that has been successfully employed for the generation of various GPCR-luciferase fusion proteins[73,74] and the nanoluciferase coding sequence. All constructs were assembled in pcDNA3.1.

Site-directed mutagenesis

Site-directed mutagenesis in TAS2R14 was performed by Transfer-PCR (TPCR), as described previously[75]. Primers used for the mutagenesis are listed in Supplementary Table 5.

Protein expression and purification

hTAS2R14, miniGα-gust-Gβ_1-Gγ_2 were co-expressed in *Sf9* cells (*Spodoptera frugiperda*) at a ratio of 1:1:1:1. The cells were cultured in ESF921 (Expression systems LLC) at 27 °C and harvested by centrifugation after 60 h. Cell pellets were lysed in a buffer containing 20 mM HEPES pH 7.4, 100 mM NaCl, 10 mM $MgCl_2$, 100 µM TCEP, protease inhibitor cocktail (PIC; 1 mM PMSF, 2.5 µg/mL leupeptine, 2 mM benzamidin), 15% glycerol and 100 µM Flufenamic acid (FFA). Complex formation was instigated at room temperature for 1 h by the addition of 50 mU/mL apyrase (Sigma), followed by membrane collection by ultracentrifugation. The membranes were then dounced and solubilized for 1.5 h at 4 °C using 0.5% (w/v) lauryl maltose neopentylglycol (LMNG, Anatrace) and 0.05% (w/v) cholesterol hemisucinate (CHS, Anatrace) in 20 mM HEPES pH 7.4, 150 mM NaCl, 10 mM $MgCl_2$, 100 µM TCEP, PIC, benzonase and 100 µM FFA. Insoluble material was removed by centrifugation at 37,000xg for 30 min, and clarified supernatant was loaded onto an α-FLAG resin (Anti-DYKDDDDK G1 affinity resin, Genescript) packed in gravity flow column. The protein-bound beads were washed with 10 column volumes (CV) of wash buffer containing 20 mM HEPES pH 7.4, 150 mM NaCl, 10 mM $MgCl_2$, 0.075% (wt/vol) LMNG, 0.025% (wt/vol) GDN (Anatrace), and 0.01% (wt/vol) CHS, 100 µM TCEP and 100 µM FFA. Bound material was eluted in a 3CV of buffer identical in composition to the wash buffer and supplemented with 0.25 mg/mL FLAG peptide (DYKDDDDK peptide, Genescript). The eluted sample was incubated overnight with 150 µg/mL ScFV16. The sample was concentrated using an Amicon Ultra Centrifugal Filter (MWCO 100 kDa, Merck-Millipore) and loaded into Superose 6 10/300 GL column (Cytiva) with a running buffer containing 20 mM HEPES pH 7.5, 150 mM NaCl, 0.00075% (wt/vol) LMNG, 0.00025% GDN, and 0.0001% (wt/vol) CHS, 10 µM FFA. The fractions corresponding to monomeric complex were collected and concentrated for the EM experiments.

ScFv16 production

Production of ScFv16 was conducted following the previously outlined methods[23]. In brief, a C-terminus 8x His tagged scFv16 with a 3 C cleavage site and a secretion tag was expressed in *Trichoplusia ni Hi5* cells (Tni, Expression systems LLC). Cells were grown for 48 h at 27 °C and harvested by centrifugation. The supernatant was collected and pH adjusted with Tris buffer to pH 8.2 and supplemented with 1 mM $NiCl_2$, 5 mM $CaCl_2$ and PIC. The solution was stirred for 1 h at room temperature (RT) and clarified by centrifugation at 4000xg for 15 min. The supernatant was loaded onto nickel resin (Cytiva) and washed with 20 mM HEPES pH 7.5, 100 mM NaCl and 20 mM imidazole. Elution was performed with 20 mM HEPES pH 7.5, 100 mM NaCl and 250 mM imidazole. The eluted protein was loaded onto a Superdex 200 10/300 GL column (Cytiva) and ran with 20 mM HEPES pH 7.4 and 100 mM NaCl. Purified fractions were pooled, concentrated, flash-frozen in the presence of 20% glycerol and kept in -80 °C until further use.

Cryo-EM

A volume of 3.5 µl of purified sample at 14 mg/mL was applied on glow-discharged (90 s, 15 mA, PELCO easiGlow, Ted Pella) holey carbon gold grids (UltrAuFoil® R1.2/1.3, 300 mesh). The grids were blotted using a Vitrobot Mark IV (FEI) with 3.5 s blotting time at 22 °C in 100% humidity, and plunge-frozen in liquid ethane. A total of 5,537 micrographs were recorded on a Titan Krios electron microscope (ThermoFisher Scientific - FEI) operating at 300 kV at a magnification of 105,000xg and corresponding to a magnified pixel size of 0.826 Å. A BioQuantum energy filter (Gatan) was operated with an energy slit width of 20 eV. Micrographs were recorded using a K3 direct electron camera (Gatan) with an exposure rate of ~30.6 $e^{-}Å^{-2}s^{-1}$ and defocus values ranging from −0.8 µm to −2.0 µm. The total exposure time was 1.49 s, and intermediate frames were recorded in 0.033 s intervals resulting in an accumulated dose of ~ 45.5 $e^{-}Å^{-2}$ and a total of 45 frames per micrograph. Automatic data acquisition was done using EPU (FEI, ThermoFisher Scientific).

Patch motion correction, CTF estimation, particle picking, 2D classification, ab-initio model reconstruction, and heterogeneous refinement were performed in cryoSPARC v4.2.1[76,77]. Homogeneous groups of particles with well-resolved features were refined using the non-uniform refinement algorithm in cryoSPARC. Particle coordinates with their assigned angles were imported into Relion 4.0[78,79] and were subjected to alignment-free 3D classification to enrich for more refined homogeneous particle populations. Selected particles were then transferred back to cryoSPARC and further refined by nonuniform refinement followed by a local refinement focused on the receptor excluding the micelle and the G-proteins, separately. A flowchart describing data-processing steps is available in Supplementary Fig. 2. The final map was reconstructed with a total of 127,503 particles and has an indicated nominal resolution of 3.03 Å. The resolution is based on the gold-standard Fourier shell correlation (FSC) using the 0.143 criterion (Supplementary Fig. 3). Angular distribution for particle projections was plotted using cryoSPARC, local resolution was determined using Phenix[80,81] and plotted using ChimeraX[82].

Model building and refinement

Initial coordinates were generated using AlphaFold2[83,84] using the hTAS2R14 sequence. Ligand coordinates and geometry restraints were generated taken from the PDB library and correspond to the previously reported structure of FFA with the human transthyretin (PDB ID: 1BM7[85]). Models were initially docked into the EM density map using ChimeraX[82], followed by iterative manual building in Coot[86,87]. The final models were subjected to global refinement and minimization in real space using phenix.real_space_refine implemented in Phenix[80,81]. The binding pose of the ligand was further validated by Gemspot[56]. MolProbity[88] was used to evaluate model geometry. The final refinement parameters are provided in Supplementary Table 1. Structures have been deposited into the PDB and Electron Microscopy Data Bank (EMDB) databases with accession codes 8RQL/EMD-19445, respectively.

Mini-Gα_{gust} recruitment assays

Human Embryonic Kidney 293 (HEK293; ATCC CRL-1573) adherent cells were cultured in 10 cm plates in Dulbecco's Modified Eagle's media (DMEM; Merck), containing 10% Fetal Bovine Serum (FBS), 1% L-glutamine amino acid, and 0.2% penicillin-streptomycin. To harvest, cells were washed with PBS, trypsinized in 1X Trypsin-EDTA (Merck), neutralized in warmed DMEM and centrifuged (1000xg) for 5 min. The resulting cell pellet was resuspended in DMEM, seeded in a 6-well plate (10^6 cells/well) and reverse transfected with 2.5 μg DNA per well of the TAS2R14-LgBiT and SmBiT-miniGα-gust plasmids at a ratio of 1:10 SmBiT-miniGα_{gus} to TAS2R14-LgBiT, using transfection reagent linear polyethyleneimine (PEI) at a 3:1 ratio of reagent to DNA. 24 h post transfection, cells were seeded (60,000 cells/well) in poly-D-lysine coated white bottom 96-well plates and incubated for 24 h at 37 °C and 5% CO_2. The following day, plates were washed with PBS equilibrated for 1 h at 37 °C with 90 μL/well of assay buffer (HBSS 1X, 24 mM HEPES pH 7.4, 3.96 mM $NaHCO_3$, 1.3 mM $CaCl_2$, and 1 mM $MgSO_4$). Furimazine (Nanolight Technology) was prepared in assay buffer at a 1:20 dilution and 25 μL of the furimazine solution was added per well. Luminescence readings were taken every minute at 37 °C until the signal was stable (3-5 min). Immediately after, 10 μl of agonist/vehicle were added and luminescence was further recorded for 40–60 min (no lens, 0.3 s integration time and 1 min intervals at 37 °C using a Clariostar® Plate Reader (BMG, Germany). Luminescence was normalized to basal, and the obtained responses were analyzed using the equation for sigmoid concentration–response curves (four-parameter) using GraphPad Prism 9.4.1 for Windows (GraphPad, USA). Per compound, three independent experiments were performed with each concentration in triplicate.

BRET G-protein dissociation assay

HEK293 cells were cultured and harvested, as previously described. Cells were seeded at 10^6 cells/well into 6-well tissue culture treated plates and reverse transfected with 1 μg plasmid DNA/well (WT/mutant receptor and TRUPATH biosensors Gα-gustRluc8, $G\beta_1$ and $G\gamma_{13}$-GFP2 at a 1:1:1:1 ratio using transfection reagent PEI at a 3:1 ratio of reagent to DNA. Plates were incubated for 24 h at 37 °C and 5% CO_2. Transfected cells were harvested and seeded at 50,000 cells/well into poly-D-lysine treated 96-well flat bottom white culture plates and grown for 24 h at 37 °C and 5% CO_2. Cells were washed then incubated in 80 μL assay buffer (1x HBSS, 24 mM HEPES, 3.96 mM $NaHCO_3$, 1.3 mM $CaCl_2$, 1 mM $MgSO_4$ and 10% w:v BSA) for 1 h at 37 °C, before acquiring basal reads at 37 °C using the Clariostar® Plus Plate Reader (BMG LabTech, Germany) equipped with 515-30 and 410-80 emission filters for GFP2 (Green Fluorescent Protein 2) and RLuc8 (Renilla Luciferase 8), respectively. Coelenterazine 400a (NanoLight Technlogies) prepared in assay buffer was added at 10 μL/well (final concentration 100 μM). Readings taken during the following 5-minute equilibration period were considered baseline measurements before the addition of 10 μL ligand or vehicle, after which readings for agonist-activity were taken for a further 7 min (0.1 s integration time). A shaking step of 300 rpm for 3 s followed the addition of coelenterazine and ligand. Raw BRET ratios were calculated as a ratio of GFP2 emission to RLuc8 emission. ΔBRET was calculated by correcting raw BRET values for vehicle. For each mutant, at least three independent concentration-response experiments were performed in triplicate. Concentration response curves were plotted using a best-fit nonlinear analysis on GraphPad Prism 9.5.0 for macOS (GraphPad, USA).

Surface expression levels (flow cytometry)

HEK293 cells were seeded and reverse transfected with wild-type/mutant TAS2R14 receptor and TRUPATH biosensors using PEI, as previously described for the G-protein dissociation assay. Cells were washed three times, harvested in ice-cold FACS buffer (1x Ca^{2+} and Mg^{2+} free DPBS, 1 mM EDTA, 25 mM HEPES, and 1% BSA) and centrifuged at 800x*g* for 5 min at 4 °C. Supernatant was aspirated and approximately 10^6 cells were resuspended in 350 μL FACS buffer containing Alexa Fluor® 488 anti-FLAG conjugated antibody (1:1000, BioLegend, 637317) and incubated for 30 min in darkness at 4 °C with agitation. Cells were then washed three times in ice-cold FACS buffer, fixed in 4% paraformaldehyde (PFA) for 20 min on ice, and washed an additional two more times in FACS buffer. Cells were strained with a 40 μM strainer and incubated with DAPI (1:10,000 ThermoFisher) for 1 min prior to analysis on a LSR Fortessa 1. Data were analysed using FlowJo v10 in which doublets were excluded and the remaining singlets were gated according to forward and side scatter profiles, with dead cells excluded using DAPI and non-transfected cells excluded based on absence of AF488 signal. Gating parameters are shown in Supplementary Fig. 6a. Three independent experiments were performed, and FlowJo v10 software (FlowJo LLC) was used to calculate median fluorescence intensities (Supplementary Fig. 6b).

NanoBRET binding assay

Membrane preparations for NLuc-TAS2R14 and TAS2R14-Nluc were obtained in analogy to previously described protocols[89]. In brief, HEK293T cells (gift from the Chair of Physiology, FAU Erlangen-Nürnberg) were grown to 50–80% confluence at 5% CO_2 in DMEM-F12 supplemented with 10% FBS, 100 μg/μL penicillin, 100 μg/μL streptomycin, and 2 mM L-glutamine at 37 °C. On transfection day, the growth medium was replaced and cells were transfected with 3-5 μg DNA per 15 cm culture dish of the secNLuc-TAS2R14 or TAS2R14-NLuc plasmids using Mirus 293 as the transfection reagent at a 3:1 reagent to DNA ratio. Cells were incubated with the transfection mixture for 24 h at 5% CO_2 and 37 °C, before the growth medium was renewed, and cells were cultured for further 24 h. For harvesting, cells were rinsed with ice-cold PBS, detached with a pipette using Tris-EDTA buffer (10 mM Tris, 0.5 mM EDTA, 5.4 mM KCl, 140 mM NaCl, pH7.4), and centrifuged (218xg) for 8 min. The pellet was resuspended in 10 mL ice-cold Tris-EDTA buffer, and cells were lysed with an Ultraturrax (20,000 rpm, 5 ×5 s). The lysate was centrifuged at 50,830xg for 18 min at 4 °C. The pellet was homogenized in membrane buffer (50 mM Tris, 1 mM EDTA, 5 mM $MgCl_2$, 100 μg/mL bacitracin, 5 μg/mL soybean trypsin inhibitor, pH 7.4) with a glass-teflon homogenizer and aliquots were shock-frozen in liquid nitrogen and stored at -80 °C until use. The total protein concentration was measured following the Lowry method[90] with bovine serum albumin as the standard.

Membrane nanoBRET saturation binding assays with secNLuc-TAS2R14 or TAS2R14-Nluc and the TP46 ligand were performed in 384-well plates in a final volume of 30 μL, and are similar to previously established protocols[39,40]. For the screening of the fluorescent probes, 15 μL of the TAS2R14 expressing HEK293T cell membranes diluted in nanoBRET buffer (50 mM Na_2HPO_4, 50 mM KH_2PO_4, pH 7.4, 1 mg/mL saponin, 5% FBS, final protein concentration 2-5 μg/well) were incubated with 5 μL of the fluorescent ligands (final concentration 1 or

5 μM) and 5 μL nanoBRET buffer or 5 μL of a solution of FFA in nanoBRET buffer (final concentration 30 μM) at 37 °C for 90 min. Directly before the BRET measurement, 5 μL of a furimazine solution (nanoBRET substrate, Promega, final dilution 1:3000) was added and bioluminescence was recorded at ambient temperature using a Clariostar® microplate reader equipped with the respective 475-30 nm and 620-10 nm emission filters. Total-BRET was calculated as the ratio of acceptor fluorescence and donor luminescence. Specific BRET was determined as the difference of total and non-specific BRET recorded in the presence of 30 μM FFA. For each ligand, 4-6 independent experiments were performed, with each concentration in triplicate. Statistical significance of the specific BRET signals was determined by comparing total and non-specific BRET for each ligand ($p < 0.05$, paired Student's t-test, Holm-Sidak correction for multiple comparisons) for the individual experiments.

Saturation binding assays with TP46 were performed in the same manner, except for the concentration of the fluorescent ligand, which was varied between 0.1 and 10 μM. Obtained BRET ratios for total, non-specific (determined in the presence of 30 μM FFA), and specific BRET were analyzed employing the algorithms for one-site saturation binding implemented PRISM10.0.3 (GraphPad, USA). A total of 5 or 7 independent experiments for the extra- and intracellularly NLuc-labeled TAS2R14 construct, respectively, were performed to determine the K_D of TP46. The TAS2R14 affinity of FFA was determined by concentration-dependent competition with TP46. Hence nanoBRET binding experiments were performed as described above, using a total protein amount of 2-5 μg/well, TP46 in a final concentration of 1–2 μM and varying the concentration of FFA from 1 nM to 300 μM. For competition experiments with cholesterol, we used a solution of cholesterol in 5 % methyl-β-cyclodextrin that was diluted in assay buffer. Obtained BRET-signals were normalized to display specific TP46 binding (total binding 100%, non-specific binding 0%) and further analyzed with the algorithms for one-site competition implemented in Graphpad Prism 10.0 to provide a K_i value based on the equation of Cheng and Prusoff[91].

Absorption (400–750 nm) and emission spectra of TP46 (100 μL, final concentration 10 μM in nanoBRET assay buffer diluted from a 1 mM DMSO stock) were collected in a half-area 96-well plate with a Clariostar® microplate reader employing the system's monochromators. For the emission spectrum (520–750 nm), an excitation wavelength of 490 nm was used. For the determination of the nanoluciferase emission spectrum, membrane preparations (secNluc-TAS2R14, 5 μg protein/well) diluted in nanoBRET buffer were incubated with furimazine (Promega, Mannheim, Germany, final dilution 1:3,000) for 2 min in the dark before bioluminescence (330–700 nm) was recorded employing the Clariostar® microplate reader. All spectra were background corrected with the respective solvent solutions and normalized to the maximum absorbance/emission of each sample.

TAS2R14 activation by LW384, the alkyne precursor of TP46 was measured in an IP_1 accumulation in HEK293T cells expressing the human TAS2R14 and a chimeric Gq_{i5} protein as described previously[36]. Responses were normalized to buffer conditions (0%), and the maximum effect of the reference agonist flufenamic acid (100%) and concentration-response curves were further analyzed using four-parameter non-linear regression (GraphPad Software, La Jolla, USA).

Chemical synthesis of fluorescent TAS2R14 ligands

Synthetic procedures were conducted using standard equipment and devices. Reactions were performed under inert atmosphere using nitrogen gas if not stated otherwise. Solvents were purchased in the highest available purity grade from Acros and Fisher Scientific and used without further purification. Dry solvents for synthetic procedures were purchased and stored in sealed septum bottles. Starting materials were purchased from abcr GmbH, BLD Pharmatecch, ChemPUR and Sigma Aldrich and used without further purification.

A synthetic scheme depicting the synthesis of the fluorescent TAS2R14 ligands is provided in Supplementary Fig. 4.

NMR-spectroscopy

NMR spectra were obtained on a Bruker Avance 400 (^{1}H at 400 MHz, ^{13}C at 101 MHz) or a Bruker Avance 600 (^{1}H at 600 MHz, ^{13}C at 151 MHz) spectrometer at 298 K using the solvents indicated. ^{13}C-NMR spectra were recorded as DEPTQ and with proton decoupling. Chemical shifts are referenced against the used NMR solvent and indicated in ppm. Multiplicities are reported as follows: s singlet; d doublet, t triplet; q quartet; quint. quintet; m multiplet. ^{13}C-NMR spectra were not recorded for the fluorescent ligands LW392, LW393 and LW394 due to the limited amount of sample.

High-resolution mass spectrometry

For the final TAMRA-containing compounds, ESI-TOF high mass accuracy and resolution experiments were performed on an AB Sciex Triple TOF660 Sciex, on a Bruker maXis MS or a Bruker timsTOF Pro.

Flash column chromatography

Purification by flash chromatography was conducted using Silica Gel 60 (40–63 μm mesh) from Merck as stationary phase.

HPLC-MS

Analytical LCMS was performed on Thermo Scientific Dionex Ultimate 3000 HPLC system using DAD detection (230 nm; 254 nm) equipped with either a Kinetex 2.6 u mesh C8 100 A (2.1 × 75 mm, 2.6 μm) HPLC column or a Zorbax Eclipse XDB-C8 (4.6 × 150 mm, 5 μm) HPLC column, using mass detection on a BRUKER amaZon SL mass spectrometer using ESI or APCI ionization source.

Preparative RP-HPLC

Purification by preparative RP-HPLC was performed on AGILENT 1260 Preparative Series equipped with a VWD detector (210 nm, 230 nm, 254 nm, 280 nm) using a Zorbax Eclipse XDB-C8 21.2 × 150 mm column with 5 μm particles [C8], flow rate 10 mL/min, employing eluent systems as specified below.

Analytical RP-HPLC

HPLC purity analyses were performed with an Agilent binary gradient system using UV detection (λ = 210, 220, 230, 254, and 280 nm) in combination with ChemStation software. A Zorbax Eclipse XDB-C8 (4.6 mm × 150 mm, 5 μm) column was used with a flow rate of 0.5 mL/min in reversed-phase mode.

eluent system 1: methanol/H_2O + 0.1% HCOOH, *gradient*: 10% for 3 min, 10% to 100% in 15 min, 100% for 6 min, 100% to 10% in 3 min, 10% for 3 min

eluent system 2: acetonitrile/H_2O + 0.1% HCOOH, *gradient*: 5% for 3 min, 5% to 95% in 15 min, 95% for 6 min, 95% to 5% in 3 min, 5% for 3 min

General procedure for the coupling of anilines with aryl halides (GP1)

In a microwave tube, the respective aryl halide, aniline, $Pd(OAc)_2$, and (±)BINAP were dissolved in dry toluene. The mixture was purged with argon and Cs_2CO_3 was added under argon flow, sealed and stirred at 120 °C. After completion, the mixture was diluted with EtOAc, washed with 2 M HCl (3x), brine (3x), dried over $MgSO_4$, filtered and evaporated. The product was purified by column chromatography.

General procedure for the deprotection of the benzyloxy phenylamino benzoate (GP2)

In an oven dried Schlenk flask, the benzyl protected phenol was dissolved in EtOH/CH_2Cl_2. After evacuating and backfilling with argon, Pd/C was added. The flask was then again evacuated and backfilled with

argon (3x), purged with H_2 and stirred at room temperature. After completion of the reaction, the mixture was filtered through a syringe filter and evaporated. Purification of the compound was achieved by column chromatography (intermediates) or preparative HPLC (final compounds).

General procedure for the Williamson ether synthesis of alkyne phenylamino benzoates (GP3)

In a microwave tube, the respective hydroxyphenylamino benzoate was dissolved in ACN or a mixture of ACN/H_2O (99.5:0.5). K_2CO_3 was added and the mixture was flushed with argon. The respective tosyl alkyl linker, tosyl polyethylene glycol linker, halogenalkyl linker or halogen polyethylene glycol linker was added and the reaction mixture was flushed with argon for further 2 min. The tube was sealed and the reaction mixture was stirred at 50 °C (if dissolved in ACN/H_2O) or 80 °C (if dissolved in ACN). After completion of the reaction the mixture was let cool to room temperature, the solvent was evaporated. The resulting residue was diluted in either DCM or EtOAc and washed with either H_2O, 2 M HCl or saturated $NaHCO_3$ solution (3x). The combined organic layers were washed with brine (3x), dried over Na_2SO_4, filtered and the solvent was evaporated. Purification was achieved by column chromatography.

General procedure for the nucleophilic substitution of bromoalkyl oxyphenylamino benzoates to azidoalkyl oxyphenylamino benzoates (GP4)

In a microwave tube, the respective bromoalkyl oxyphenylamino benzoate was dissolved in ACN/H_2O (10:1) before NaN_3 was added to the solution. The tube was sealed and the reaction was stirred at 82 °C. After completion of the reaction, the mixture was let cool to room temperature. The solvent was evaporated and the residue diluted with CH_2Cl_2. The solution was extracted with a saturated $NaHCO_3$ solution (3x) and the combined organic layers were dried over Na_2SO_4, filtered and evaporated. Further purification was either achieved by column chromatography or not necessary.

General procedure for the hydrolysis of phenylamino benzoates (GP5)

In a microwave tube, the respective phenylamino benzoate was dissolved in a mixture of MeOH/H_2O, MeOH/THF/H_2O, or EtOH/H_2O or EtOH/THF/H_2O. After addition of KOH or 2 M NaOH, the tube was sealed and the mixture was stirred either at room temperature or reflux. After completion of the reaction, the mixture was let cool to room temperature, the solvent was evaporated and the residue dissolved in CH_2Cl_2 or EtOAc. The mixture was acidified to pH 1 using 2 M HCl and the aqueous layer was extracted using CH_2Cl_2 (3x) or EtOAc (3x). The combined organic layers were washed with brine (3x), dried over Na_2SO_4, filtered and evaporated. Final purification was achieved by flash chromatography (intermediates) or preparative HPLC.

General procedure for 1,3-dipolar cycloadditions (GP6)

The respective azide was dissolved in *t*BuOH/H_2O (1:1) and added to ta microwave tube containing the respective alkyne. DMF and TBTA (Tris[(1-benzyl-1*H*-1,2,3-triazol-4-yl)methyl]amine)) were added. Freshly prepared 1 M $CuSO_4 \cdot 5\ H_2O$ and 1 M sodium ascorbate solutions were added. The tube was sealed and the mixture was stirred either at room temperature. After the reaction was finished the solvent was evaporated and the residue was dissolved in MeOH and purified via column chromatography (intermediates) or via preparative HPLC (final compounds).

General procedure for the amide coupling of 6-TAMRA and aminolinkers (GP7)

To a solution of TBTU in DMF, DIPEA was added, and the mixture was added to a cooled solution of TAMRA in DMF. The reaction mixture then was cooled to 0 °C and stirred for 15 min. The respective amine was added to the solution, the microwave was sealed, and the mixture was stirred at room temperature. After completion of the reaction, the solvent was evaporated and the crude product was purified using column chromatography (dichloromethane/MeOH).

Molecular dynamics simulations

The experimental structure was used to set up MD simulations. The TAS2R14 receptor with the α-subunit of the associated G-protein and with FFA in both binding sites was used for the complex trajectories, and receptor without ligands and G-protein was used as a starting point for simulating apo trajectories.

Missing loops, side chains, and hydrogen atoms were added using the Protein preparation wizard and the Crosslink protein tools in the Schrödinger suite (Schrödinger Release 2021-1, LLC, New York, NY, 2021). All Histidine protonation states were determined using MolProbity[92]. The CHARMM-GUI input generator[93–96] was then used to prepare the initial structures for the MD runs. The receptor was embedded within a POPC membrane bilayer (using 460 molecules), where the protein orientation was determined by the PPM web server[97]. The receptor along with the α-subunit of the associated G-protein were capped with standard N- and C-termini. The proteins, lipids, and ligands were then solvated using ~55,000 CHARMM-TIP3P water molecules and NaCl ions were added to a total concentration of 150 mM. The simulation box dimensions were ~ 126A*126A*151A. The Charmm36m force-field[98,99] was used for all other components. Analyses were performed with VMD 1.9.3[100]. A file with the coordinates of one replica after 200 ns of production run and the input *mdp file used for the production run are provided as supplementary files.

Each complex was energy minimized in five steps as outlined in Supplementary Table 2 by the steepest descent protocol. In each step, the positional restraints on proteins and lipids were gradually removed (see Supplementary Table 2). Then, six steps of equilibration were performed, whereby the positional restraints were also progressively decreased (Supplementary Table 3). During equilibration, the temperature was held constant at 310 K using the Berendsen thermostat with a coupling time constant of 1 ps. At part of the equilibration stage, the pressure was held constant at 1 atm using a semi-isotropic Berendsen barostat with a coupling constant of 5 ps. After a total equilibration time of 10.875 ns, production runs in the NVT ensemble were run for at least 200 ns with a 2 fs time step at a temperature of $T = 310$ K. During production, the temperature was held constant using a Nosé-Hoover thermostat. Throughout, bond lengths to hydrogen atoms were constrained using LINCS. Short-range electrostatic and van der Waals interactions were cut off at 1.2 nm, while long-range electrostatic interactions were computed using the particle mesh Ewald method. Periodic boundaries were employed. Gromacs *mdp input file for the production run and a representative snapshot after 200 ns production run is available as Supplementary Data 1 and 2.

Reporting summary

Further information on research design is available in the Nature Portfolio Reporting Summary linked to this article.

Data availability

The cryo-EM density map has been deposited in the Electron Microscopy Data Bank (EMDB) under accession code EMD-19445, and model coordinates have been deposited in the Protein Data Bank (PDB) under accession number 8RQL. All other data are available in the manuscript or supplementary materials. Source data are provided with this paper.

References

1. Meyerhof, W. et al. The molecular receptive ranges of human TAS2R bitter taste receptors. *Chem. Senses* **35**, 157–170 (2009).

2. Di Pizio, A. et al. Comparing class A GPCRs to bitter taste receptors: Structural motifs, ligand interactions and agonist-to-antagonist ratios. *Methods Cell Biol.* **132**, 401–427 (2016).
3. Di Pizio, A. & Niv, M. Y. Promiscuity and selectivity of bitter molecules and their receptors. *Bioorg. Med. Chem.* **23**, 4082–4091 (2015).
4. Dagan-Wiener, A. et al. BitterDB: taste ligands and receptors database in 2019. *Nucleic Acids Res* **47**, 1179–1185 (2019).
5. Delompré, T., Belloir, C., Martin, C., Salles, C. & Briand, L. Detection of bitterness in vitamins is mediated by the activation of bitter taste receptors. *Nutrients* **14**, 4141 (2022).
6. Roland, W. S. U. et al. Bitter taste receptor activation by flavonoids and isoflavonoids: Modeled structural requirements for activation of hTAS2R14 and hTAS2R39. *J. Agric. Food Chem.* **61**, 10454–10466 (2013).
7. Behrens, M. et al. The human taste receptor hTAS2R14 responds to a variety of different bitter compounds. *Biochem. Biophys. Res. Commun.* **319**, 479–485 (2004).
8. Levit, A. et al. The bitter pill: clinical drugs that activate the human bitter taste receptor TAS2R14. *FASEB J.* **28**, 1181–1197 (2014).
9. Margulis, E. et al. Bitter odorants and odorous bitters: toxicity and human TAS2R targets. *J. Agric. Food Chem.* **71**, 9051–9061 (2023).
10. Grassin-delyle, S. et al. The expression and relaxant effect of bitter taste receptors in human bronchi. *Respir. Res.* **14**, 1–14 (2013).
11. Yan, C. H. et al. Nitric oxide production is stimulated by bitter taste receptors ubiquitously expressed in the sinonasal cavity. *Am. J. Rhinol. Allergy* **38**, 85–92 (2017).
12. Bloxham, C. J., Foster, S. R., Thomas, W. G. & Thomas, W. G. A bitter taste in your heart. *Front. Physiol.* **11**, 431 (2020).
13. Bloxham, C. J. et al. Cardiac human bitter taste receptors contain naturally occurring variants that alter function. *Biochem. Pharmacol.* **219**, 115932 (2023).
14. Liszt, K. I. et al. Caffeine induces gastric acid secretion via bitter taste signaling in gastric parietal cells. *Proc. Natl Acad. Sci. USA* **114**, E6260–E6269 (2017).
15. Gentiluomo, M. et al. Taste receptor polymorphisms and male infertility. *Hum. Reprod.* **32**, 2324–2331 (2017).
16. Jaggupilli, A. et al. Analysis of the expression of human bitter taste receptors in extraoral tissues. *Mol. Cell. Biochem.* **426**, 137–147 (2017).
17. Singh, N., Shaik, F. A., Myal, Y. & Chelikani, P. Chemosensory bitter taste receptors T2R4 and T2R14 activation attenuates proliferation and migration of breast cancer cells. *Mol. Cell. Biochem.* **465**, 199–214 (2020).
18. Miller, Z. A. et al. Lidocaine induces apoptosis in head and neck squamous cell carcinoma cells through activation of bitter taste receptor T2R14. *Cell Rep.* **42**, 113437 (2023).
19. Stern, L. et al. Potential role of the bitter taste receptor T2R14 in the prolonged survival and enhanced chemoresponsiveness induced by apigenin. *Int. J. Oncol.* **62**, 1–14 (2023).
20. Mclaughlin, S. K., Mckinnon, P. J. & Margolskee, R. F. Gustducin is a taste-cell-specific G protein closely related to the transducins. *Nature* **357**, 563–569 (1992).
21. Xu, W. et al. Structural basis for strychnine activation of human bitter taste receptor TAS2R46. *Science* **377**, 1298–1303 (2022).
22. Di Pizio, A. et al. Rational design of agonists for bitter taste receptor TAS2R14: from modeling to bench and back. *Cell. Mol. Life Sci.* **77**, 531–542 (2019).
23. Maeda, S. et al. Development of an antibody fragment that stabilizes GPCR/G-protein complexes. *Nat. Commun.* **9**, 1–9 (2018).
24. Israeli, H. et al. Structure reveals the activation mechanism of the MC4 receptor to initiate satiation signaling. *Science* **372**, 808–814 (2021).
25. Kim, K. et al. Structure of a hallucinogen-activated Gq-coupled 5-HT2A serotonin receptor. *Cell* **182**, 1574–1588.e19 (2020).
26. Koehl, A. et al. Structure of the μ-opioid receptor-Gi protein complex. *Nature* **558**, 547–552 (2018).
27. Carpenter, B. et al. Mini-G proteins: novel tools for studying GPCRs in their active conformation. *PLoS ONE* **12**, 1–26 (2017).
28. Dixon, A. S. et al. NanoLuc complementation reporter optimized for accurate measurement of protein interactions in cells. *ACS Chem. Biol.* **11**, 400–408 (2016).
29. Inoue, A. et al. Illuminating G-protein-coupling selectivity of GPCRs. *Cell* **177**, 1933–1947.e25 (2019).
30. Olsen, R. H. J. et al. TRUPATH, an open-source biosensor platform for interrogating the GPCR transducerome. *Nat. Chem. Biol.* **16**, 841–849 (2020).
31. Galés, C. et al. Probing the activation-promoted structural rearrangements in preassembled receptor – G protein complexes. *Nat. Struct. Mol. Biol.* **13**, 778–786 (2006).
32. Duan, J. et al. Cryo-EM structure of an activated VIP1 receptor-G protein complex revealed by a NanoBiT tethering strategy. *Nat. Commun.* **11**, 1–10 (2020).
33. Whitwell, E. Flufenamic acid in rheumatoid arthritis. *Ann. Rheum. Dis.* **26**, 43–46 (1967).
34. Hall, M. P. et al. Engineered luciferase reporter from a deep sea shrimp utilizing a novel imidazopyrazinone substrate. *ACS Chem. Biol.* **7**, 1848–1857 (2012).
35. England, C. G., Ehlerding, E. B. & Cai, W. NanoLuc: a small luciferase is brightening up the field of bioluminescence. *Bioconjug. Chem.* **27**, 1175–1187 (2016).
36. Waterloo, L. et al. Discovery of 2-aminopyrimidines as potent agonists for the bitter taste receptor TAS2R14. *J. Med. Chem.* **66**, 3499–3521 (2023).
37. Rostovtsev, V. V., Green, L. G., Fokin, V. V. & Sharpless, K. B. A stepwise huisgen cycloaddition process: copper(I)-catalyzed regioselective 'ligation' of azides and terminal alkynes. *Angew. Chem. - Int. Ed.* **41**, 2596–2599 (2002).
38. Stoddart, L. A. et al. Application of BRET to monitor ligand binding to GPCRs. *Nat. Methods* **12**, 661–663 (2015).
39. Huber, M. E. et al. A chemical biology toolbox targeting the intracellular binding site of CCR9: fluorescent ligands, new drug leads and PROTACs. *Angew. Chem. - Int. Ed.* **61**, e202116782 (2022).
40. Allikalt, A. et al. Fluorescent ligands for dopamine D2/D3 receptors. *Sci. Rep.* **10**, 1–13 (2020).
41. Rosier, N. et al. A versatile sub-nanomolar fluorescent ligand enables nanoBRET Binding studies and single-molecule microscopy at the histamine H3 receptor. *J. Med. Chem.* **64**, 11695–11708 (2021).
42. Kim, Y. et al. Bitter taste receptor activation by cholesterol and an intracellular tastant. *Nature* **628**, 664–671 (2024).
43. Hu, X. et al. Bitter taste TAS2R14 activation by intracellular tastants and cholesterol. *Nature* **631**, 459–466 (2024).
44. Tao, L. et al. Bitter taste receptor TAS2R14 activation and G protein assembly by an intracellular agonist. *Cell Res.* https://doi.org/10.1038/s41422-024-00995-4. (2024)
45. Luchetti, G. et al. Cholesterol activates the G-protein coupled receptor Smoothened to promote Hedgehog signaling. *Elife* **5**, 1–e20304 (2016).
46. Jakub, J. & El-Fakahany, E. E. Allosteric modulation of GPCRs of class a by cholesterol. *Int. J. Mol. Sci.* **22**, 1953 (2021).
47. Shaik, F. A., Medapati, M. R. & Chelikani, P. Cholesterol modulates the signaling of chemosensory bitter taste receptor t2r14 in human airway cells. *Am. J. Physiol. - Lung Cell. Mol. Physiol.* **316**, L45–L57 (2019).
48. Guixà-González, R. et al. Membrane cholesterol access into a G-protein-coupled receptor. *Nat. Commun.* **8**, 14505 (2017).
49. Fierro, F. et al. Inhibiting a promiscuous GPCR: iterative discovery of bitter taste receptor ligands. *Cell. Mol. Life Sci.* **80**, 1–17 (2023).

50. Ballesteros, J. A. & Weinstein, H. [19] Integrated methods for the construction of three-dimensional models and computational probing of structure-function relations in G protein-coupled receptors. *Methods Neurosci.* **25**, 366–428 (1995).
51. Kumar, K. K. et al. Structure of a signaling cannabinoid receptor 1-G article structure of a signaling cannabinoid receptor 1-G protein complex. *Cell* **176**, 448–458.e12 (2019).
52. Venkatakrishnan, A. J. et al. Molecular signatures of G-protein-coupled receptors. *Nature* **494**, 185–194 (2013).
53. Nowak, S. et al. Reengineering the ligand sensitivity of the broadly tuned human bitter taste receptor TAS2R14. *Biochim. Biophys. Acta - Gen. Subj.* **1862**, 2162–2173 (2018).
54. Pronin, A. N. et al. Identification of Ligands for Two Human Bitter T2R Receptors. *Chem. Senses* **29**, 583–593 (2004).
55. Born, S., Levit, A., Niv, M. Y., Meyerhof, W. & Behrens, M. The human bitter taste receptor TAS2R10 is tailored to accommodate numerous diverse ligands. *J. Neurosci.* **33**, 201–213 (2013).
56. Robertson, M. J., van Zundert, G. C. P., Borrelli, K. & Skiniotis, G. GemSpot: a pipeline for robust modeling of ligands into Cryo-EM maps. *Structure* **28**, 707–716.e3 (2020).
57. Zheng, Y. et al. Structure of CC chemokine receptor 2 with orthosteric and allosteric antagonists. *Nature* **540**, 458–461 (2016).
58. Saha, S. & Shukla, A. K. The inside story: crystal structure of the chemokine receptor CCR7 with an intracellular allosteric antagonist. *Biochemistry* **59**, 12–14 (2020).
59. Oswald, C. et al. Intracellular allosteric antagonism of the CCR9 receptor. *Nature* **450**, 462–465 (2016).
60. Liu, K. et al. Structural basis of CXC chemokine receptor 2 activation and signalling. *Nature* **585**, 135–140 (2020).
61. Lees, J. A. et al. An inverse agonist of orphan receptor GPR61 acts by a G protein-competitive allosteric mechanism. *Nat. Commun.* **14**, 5938 (2023).
62. Liu, X. et al. Mechanism of intracellular allosteric β2AR antagonist revealed by X-ray crystal structure. *Nature* **548**, 480–484 (2017).
63. Duan, J. et al. GPCR activation and GRK2 assembly by a biased intracellular agonist. *Nature* **620**, 676–681 (2023).
64. Kobayashi, K. et al. Class B1 GPCR activation by an intracellular agonist. *Nature* **618**, 1085–1093 (2023).
65. Zhao, L.-H. et al. Conserved class B GPCR activation by a biased intracellular agonist. *Nature* **621**, 635–641 (2023).
66. Jazayeri, A. et al. Structure of class B GPCR corticotropin- releasing factor receptor 1. *Nature* **199**, 438–443 (2013).
67. Ping, Y. Q. et al. Structures of the glucocorticoid-bound adhesion receptor GPR97–Go complex. *Nature* **589**, 620–626 (2021).
68. Greene, T. A. et al. Probenecid inhibits the human bitter taste receptor TAS2R16 and suppresses bitter perception of salicin. *PLoS ONE* **6**, e20123 (2011).
69. Peri, I. et al. Rapid entry of bitter and sweet tastants into liposomes and taste cells: implications for signal transduction. *Am. J. Physiol. Physiol.* **278**, 17–25 (2000).
70. Wan, Q. et al. Mini G protein probes for active G protein – coupled receptors (GPCRs) in live cells. *J. Biol. Chem.* **293**, 7466–7473 (2018).
71. Unger, T., Jacobovitch, Y., Dantes, A., Bernheim, R. & Peleg, Y. Applications of the Restriction Free (RF) cloning procedure for molecular manipulations and protein expression. *J. Struct. Biol.* **172**, 34–44 (2010).
72. Gibson, D. G. et al. Enzymatic assembly of DNA molecules up to several hundred kilobases. *Nat. Methods* **6**, 343–345 (2009).
73. Budzinski, J. et al. Bivalent ligands promote endosomal trafficking of the dopamine D3 receptor-neurotensin receptor 1 heterodimer. *Commun. Biol.* **4**, 1–13 (2021).
74. Urizar, E. et al. CODA-RET reveals functional selectivity as a result of GPCR heteromerization. *Nat. Chem. Biol.* **7**, 624–630 (2011).
75. Erijman, A., Dantes, A., Bernheim, R., Shifman, J. M. & Peleg, Y. Transfer-PCR (TPCR): a highway for DNA cloning and protein engineering. *J. Struct. Biol.* **175**, 171–177 (2011).
76. Punjani, A., Rubinstein, J. L., Fleet, D. J. & Brubaker, M. A. CryoSPARC: algorithms for rapid unsupervised cryo-EM structure determination. *Nat. Methods* **14**, 290–296 (2017).
77. Punjani, A., Zhang, H. & Fleet, D. J. Non-uniform refinement: adaptive regularization improves single-particle cryo-EM reconstruction. *Nat. Methods* **17**, 1214–1221 (2020).
78. Kimanius, D., Dong, L., Sharov, G., Nakane, T. & Scheres, S. H. W. New tools for automated cryo-EM single-particle analysis in RELION-4.0. *Biochem. J.* **478**, 4169–4185 (2021).
79. Scheres, S. H. W. *Processing of Structurally Heterogeneous Cryo-EM Data in RELION. Methods in Enzymology*. Vol. 579 (Elsevier Inc., 2016).
80. Afonine, P. V. et al. Real-space refinement in PHENIX for cryo-EM and crystallography. *Acta Crystallogr. Sect. D Struct. Biol.* **74**, 531–544 (2018).
81. Liebschner, D. et al. Macromolecular structure determination using X-rays, neutrons and electrons: recent developments in Phenix. *Acta Crystallogr. Sect. D Struct. Biol.* **75**, 861–877 (2019).
82. Meng, E. C. et al. UCSF ChimeraX: tools for structure building and analysis. *Protein Sci.* **32**, 1–13 (2023).
83. Jumper, J. et al. Highly accurate protein structure prediction with AlphaFold. *Nature* **596**, 583–589 (2021).
84. Varadi, M. et al. AlphaFold Protein Structure Database: massively expanding the structural coverage of protein-sequence space with high-accuracy models. *Nucleic Acids Res.* **50**, D439–D444 (2022).
85. Peterson, S. A. et al. Inhibiting transthyretin conformational changes that lead to amyloid fibril formation. *Proc. Natl Acad. Sci. USA* **95**, 12956–12960 (1998).
86. Emsley, P., Lohkamp, B., Scott, W. G. & Cowtan, K. Features and development of coot. *Acta Crystallogr. Sect. D Biol. Crystallogr.* **66**, 486–501 (2010).
87. Jones, T. A. Interactive electron-density map interpretation: from INTER to O. *Acta Crystallogr. Sect. D Biol. Crystallogr.* **60**, 2115–2125 (2004).
88. Williams, C. J. et al. MolProbity: more and better reference data for improved all-atom structure validation. *Protein Sci.* **27**, 293–315 (2018).
89. Möller, D. et al. Discovery of G protein-biased dopaminergics with a pyrazolo[1,5-a]pyridine substructure. *J. Med. Chem.* **60**, 2908–2929 (2017).
90. Lowry, O. H., Rosebrough, N. J., Farr, A. L. & Randall, R. J. Protein measurement with the Folin phenol reagent. *J. Biol. Chem.* **193**, 265–275 (1951).
91. Cheng, Y.-C. & Prusoff, W. H. Relationship between the inhibition constant (KI) and the concentration of inhibitor which causes 50 per cent inhibition (I50) of an enzymatic reaction. *Biochem. Pharmacol.* **22**, 3099–3108 (1973).
92. Chen, V. B. et al. MolProbity: all-atom structure validation for macromolecular crystallography. *Acta Crystallogr. Sect. D Biol. Crystallogr.* **66**, 12–21 (2010).
93. Jo, S., Kim, T., Iyer, V. G. & Im, W. CHARMM-GUI: a web-based graphical user interface for CHARMM. *J. Comput. Chem.* **29**, 1859–1865 (2008).
94. Brooks, B. R. et al. CHARMM: the biomolecular simulation program. *J. Comput. Chem.* **30**, 1545–1614 (2009).
95. Lee, J. et al. CHARMM-GUI input generator for NAMD, gromacs, amber, openmm, and CHARMM/OpenMM simulations using the CHARMM36 additive force field. *Biophys. J.* **110**, 641a (2016).
96. Wu, E. L. et al. CHARMM-GUI membrane builder toward realistic biological membrane simulations. *J. Comput. Chem.* **35**, 1997–2004 (2014).

97. Lomize, M. A., Pogozheva, I. D., Joo, H., Mosberg, H. I. & Lomize, A. L. OPM database and PPM web server: Resources for positioning of proteins in membranes. *Nucleic Acids Res* **40**, 370–376 (2012).
98. Huang, J. et al. CHARMM36m: an improved force field for folded and intrinsically disordered proteins. *Nat. Methods* **14**, 71–73 (2017).
99. Lindahl, E., Bjelkmar, P., Larsson, P., Cuendet, M. A. & Hess, B. Implementation of the charmm force field in GROMACS: Analysis of protein stability effects from correction maps, virtual interaction sites, and water models. *J. Chem. Theory Comput.* **6**, 459–466 (2010).
100. Humphrey, W., Dalke, A. & Schulten, K. VMD: Visual molecular dynamics. *J. Mol. Graph.* **14**, 33–38 (1996).

Acknowledgements

This work was funded by the European Union's Horizon 2020 research and innovation program under the European Research Council (ERC; grant no. 949364) to M.S.-B, the German Research Foundation Grants Gm 13/12 to P.G. and M.Y.N, the Israel Science Foundation grant 1129/19 to M.Y.N and Pancreatic Cancer Research Fund, the UKRI BBSRC, UUKi and the Weizmann Institute - UK joint research program to P.J.M and M.S.-B. M.S.-B. holds the Tauro Career Development Chair in Biomedical Research. M.S.-B. is supported by the Zuckerman STEM Leadership Program, the Ilse Katz Institute for Material Sciences and Magnetic Resonance Research, the Helen and Milton A. Kimmelman Center for Biomolecular Structure and Assembly, the Joseph and Wolf Lebovic Lab, the Dov and Ziva Rabinovich Endowed Fund for Structural Biology, the Harmstieg New Scientist Fund, and the Pearl Welinsky Merlo Foundation and by P. and T. Gardner. L.P. was partially supported by Excellence Fellowship from the Hebrew University Center for Nanoscience and Nanotechnology and COST Action 18133-ERNEST STSM grant. D.R.H. was supported by a British Heart Foundation project grant and fellowship. We thank Khajidmaa Flad for the cloning of the secNLuc-TAS2R14 construct, and Michael Naim, Asa Tirosh, Evgenii Ziaikin, and George Chalhoub for helpful discussions. We thank Nadav Elad for technical support with microscope operation.

Author contributions

M.Y.N. and M.S.-B. conceptualized the study; M.Y.N., M.S.-B., P.J.M., D.W., and P.G. designed the methodology; L.P. and D.M. prepared the TAS2R14-gustducin complex under the supervision of M.S.-B.; D.M. prepared grids, obtained cryo-EM data, processed data, and modeled the structure under the supervision of M.S.-B.; Y.P. cloned TAS2R14 constructs and mutants. L.P. performed and analyzed complementation assays in HEK293 cells and optimization of TRUPATH assays under the supervision of M.Y.N. and P.J.M. D.R.H. performed the TRUPATH assays and analyzed the surface expression of receptors by means of flow cytometry analysis under the supervision of P.J.M.; A.R. performed computational docking and binding site analysis under the supervision of M.Y.N. F.F., L.P., A.R., M.Y.N. and D.M. designed mutants; F.F. and L.S. performed molecular dynamics simulations under supervision of M.Y.N.; T.P. and L.W. synthesized the fluorescent ligands under the supervision of P.G.; H.H. performed functional and binding assays; D.W. designed and performed binding assays; M.S.-B., L.P. and M.Y.N. wrote the manuscript with the help of D.M., D.W., and D.R.H.; All authors provided input for the final manuscript version.

Competing interests

The authors declare no competing interests

Additional information

Supplementary information The online version contains supplementary material available at https://doi.org/10.1038/s41467-024-54157-6.

Correspondence and requests for materials should be addressed to Dorothee Weikert, Masha Y. Niv or Moran Shalev-Benami.

Peer review information *Nature Communications* thanks Osamu Nureki, Andrea Vernall and the other, anonymous, reviewer(s) for their contribution to the peer review of this work. A peer review file is available.